Atmospheric
Chemistry
and Physics

Climatology of aerosol properties at an atmospheric monitoring site on the northern California coast

Erin K. Boedicker[1,2], Elisabeth Andrews[1,2], Patrick J. Sheridan[2], and Patricia K. Quinn[3]

[1]Cooperative Institute for Research in Environmental Sciences (CIRES),
University of Colorado, Boulder, CO USA
[2]Global Monitoring Laboratory, NOAA, Boulder, CO USA
[3]Pacific Marine Environmental Laboratory, NOAA, Seattle, WA USA

Correspondence: Erin K. Boedicker (erin.boedicker@noaa.gov)

Abstract. Between April 2002 and June 2017, the Global Monitoring Laboratory (GML) of the National Oceanic and Atmospheric Administration (NOAA) made continuous measurements of a suite of in situ aerosol optical properties at a long-term monitoring site near Trinidad Head (THD), California. In addition to aerosol optical properties, between 2002–2006 a scanning humidograph system was operated, and inorganic ion and total aerosol mass concentrations were obtained from filter measurements. A combined analysis of these datasets demonstrates consistent patterns in aerosol climatology and highlights changes in sources throughout the year. THD is predictably dominated by sea salt aerosols; however, marine biogenic aerosols are the largest contributor to PM_1 in the warmer months. Additionally, a persistent combustion source appears in the winter, likely a result of wintertime home heating. While the influences of local anthropogenic sources from vehicular and marine traffic are visible in the optical aerosol data, their influence is largely dictated by the wind direction at the site. Comparison of the THD aerosol climatology to that reported for other marine sites shows that the location is representative of clean marine measurements, even with the periodic influence of anthropogenic sources.

1 Introduction

Aerosol particles affect the radiative balance both by scattering and absorbing solar radiation and by influencing the properties of clouds (IPCC, 2013). In order to separate out the contribution of anthropogenic aerosol to aerosol radiative forcing, the impact of natural aerosol particles must also be quantified (Andreae, 2007). Because the Earth's surface is dominated by oceans, marine aerosols are a dominant contributor to natural background aerosol levels (Murphy et al., 1998; Jaeglé et al., 2011), although their contribution is variable in time and space. Marine aerosols can be generated both through wave breaking – which generates sea salt aerosols consisting of both soluble ions and organic material – and through gas-to-particle conversion of volatile organic compounds (VOCs) generated by biogenic activity, leading to marine biogenic aerosols (O'Dowd and de Leeuw,

2007; Fitzgerald, 1991). The aerosol in coastal regions may be subject to significant impacts from local and/or regional anthropogenic sources, as well as long-range transport, particularly in the Northern Hemisphere (Andreae, 2007); this can make it difficult to definitively characterize the natural marine aerosol. Understanding the marine aerosol is critical not only for assessing direct aerosol forcing of a major natural aerosol type but also because marine aerosol plays a key role in cloud formation over much of the globe (Mayer et al., 2020; Hodshire et al., 2019; Carslaw et al., 2010).

Measurements over the open ocean (where anthropogenic influence is less pronounced) typically require mobile platforms such as instrumented ships or aircraft, so remote coastal locations are often used as a surrogate for sampling the marine atmosphere (O'Dowd et al., 2014; Bates et al., 1998; Brunke et al., 2004; Wood et al., 2015). An advantage that surface-based coastal site measurements have over sam-

pling from mobile platforms is that long-term, continuous information can be obtained, allowing for the development of representative climatologies on variable timescales (diurnal to annual) and the evaluation of long-term trends. Such measurements can then be used to evaluate models, but whether the measurements are representative of a clean marine environment should also be assessed (O'Dowd et al., 2014; Wang et al., 2018).

An established, long-term observatory can provide a platform for multiple instrument suites probing different aspects of the atmosphere. Long-term atmospheric monitoring deployments are (typically) limited in measurement scope to robust and proven standalone techniques, which is in contrast to field campaign efforts, which frequently utilize state-of-the-art and/or prototype instruments that only need to be operated for a short time and are attended by on-site scientists. Long-term datasets of atmospheric constituents provide an opportunity to describe inter-annual variability and climatology on a variety of timescales, to identify trends, and to develop a robust understanding of relationships amongst the measured parameters, which may not be possible from short-term studies. Analyses of extended time series of atmospheric data can be used to provide a context for field campaign observations (Brock et al., 2011; Leaitch et al., 2020), assess model simulations (Spracklen et al., 2010; Browse et al., 2012), evaluate the effectiveness of pollution control legislation and exposures (Murphy et al., 2008), and answer scientific questions related to sources, atmospheric processes, and the impacts of extreme events (Sorribas et al., 2015; Hallar et al., 2015).

In April 2002, a surface monitoring site was established at Trinidad Head (THD), near the small town of Trinidad on the northern coast of California, in order to study properties of atmospheric constituents (e.g., aerosol particles and ozone) entering the USA prior to influence by North American sources. The start of measurements at THD coincided with the 1-month intensive field campaign, Intercontinental Transport and Chemical Transformation (ITCT 2K2), aimed at understanding how (relatively) short-lived species such as aerosol particles can be transported and detected far from their source and how these species change during transport (Parrish et al., 2004). While it was found that surface measurements at THD were not ideal for studying long-range transport (VanCuren et al., 2005), it was a reasonable location for making measurements of the clean marine environment. Thus, the site remained active with a smaller suite of measurements as a long-term National Oceanic and Atmospheric Administration (NOAA) Global Monitoring Laboratory (GML) monitoring site for an additional 15 years and closed down in June 2017. This paper focuses on an analysis of surface aerosol measurements observed at THD over the 2002–2017 period of measurements and addresses two main questions in the context of remote marine observations:

1. What is the climatology (seasonal and diurnal cycles) of the aerosol chemical and optical properties at THD?

2. Are there any systematic relationships between the aerosol chemical composition and aerosol optical properties?

The discussion of these results assesses implications in terms of aerosol sources and how well THD represents a clean marine site.

2 Methods

The measurements described here were conducted at the atmospheric monitoring station on Trinidad Head, California (41.054° N, 125.151° W; 107 m a.s.l. – above sea level). The site is ~ 370 km (~ 230 miles) north of the San Francisco Bay area (population ~ 8.7 million) and ~ 350 km (~ 220 miles) south of Eugene, Oregon (population $\sim 170\,000$), making it a location relatively remote from large local and regional sources of anthropogenic pollution (Fig. 1). The site is ~ 22 km (~ 13.5 miles) north of the smaller city of Arcata (population $\sim 19\,000$) and directly southwest of the city of Trinidad (population ~ 300). Aerosol chemical filters were collected over a 4-year period from 15 April 2002–May 2006, and the aerosol optical measurements reported here cover a ~ 15-year period from 15 April 2002–1 June 2017. Other measurements took place over more limited time frames. Table 1 describes the aerosol instruments operated at Trinidad Head (THD) and their periods of operation.

2.1 Aerosol inlet system

The aerosol inlet and system at THD are the standard NOAA design and have been described in detail in other papers (Sheridan et al., 2001; Delene and Ogren, 2002; Sherman et al., 2015), so only a brief description is given here. The sampling stack was 10 m tall, constructed of 8 in. (20.32 cm) inner diameter PVC (polyvinyl chloride) pipe. A rain hat prevented precipitation from entering sample stack; the rain hat design was changed in March 2010. A total airflow of ~ 1000 L min^{-1} entered the stack. Most of this airflow (850 L min^{-1}) was excess air, while the remaining 150 L min^{-1}, the sample flow, was pulled through a gently heated 2 in. (5.08 cm) stainless-steel pipe at the base of the sampling stack and fed into a five-port flow splitter. The heating applied to the stainless-steel tube was used to lower the relative humidity (RH) of the sample to comply with Global Atmosphere Watch (GAW) sampling protocols of keeping sample RH below 40 % (WMO/GAW, 2016). At THD, 30 L min^{-1} of the splitter sample flow was routed to the aerosol optical properties measurement system, 30 L min^{-1} went to the chemical filter measurements, and 30 L min^{-1} was used to monitor the RH in the stainless-steel inlet and control the heat to lower that RH when necessary.

Table 1. Instrumentation at Trinidad Head.

Instrument	Make and/or model	Measurement	Time period (mm/yyyy)
Condensation nuclei counter (CNC)	TSI 3760	Aerosol number concentration (N) Size range particle diameter > 14 nm	04/2002–06/2017
Nephelometer[1,2]	TSI 3563	Aerosol light scattering (σ_{sp}) and backwards (σ_{bsp}) at three wavelengths (450, 550, and 700 nm)	04/2002–06/2017
Particle soot absorption photometer (PSAP)[1,2]	Radiance Research	Aerosol light absorption (σ_{ap}) at 565 nm (reported at 550 nm)	04/2002–10/2005
Particle soot absorption photometer (PSAP)[1,2]	Radiance Research	Aerosol light absorption (σ_{ap}) at three wavelengths (467, 530, and 660 nm)	10/2005–06/2013
Continuous light absorption photometer (CLAP)[1,2]	NOAA/GML	Aerosol light absorption (σ_{ap}) at three wavelengths (467, 528, and 652 nm)	12/2011–06/2017
Anemometer	RM Young	Wind data (direction and speed) at 10 m	09/2007–06/2017
Resistance temperature detector (RTD)	Logan 4150 in aspirated enclosure	Ambient temperature at 2 and 10 m	09/2007–06/2017
Relative humidity probe[3]	RM Young 41382 in aspirated enclosure	Ambient relative humidity at 2 m	08/2013–06/2017
Barometer	Setra 270	Ambient pressure	09/2007–06/2017
Chemical filters	NOAA/PMEL	Common aerosol ions, including SO_4^{-2}, NH_4^+, Cl^-, Br^-, Na^+, K^+, Ca^+, Mg^+, NO^{3-}, MSA^-, and oxalate	04/2002–05/2006

[1] These measurements measured at two size cuts, namely PM_1 and PM_{10}. [2] Correction methods used for these instruments are outlined in Anderson and Ogren (1998) for the nephelometer and Bond et al. (1999) and Ogren (2010) for the PSAP and CLAP. [3] Ambient RH measurements prior to August 2013 were invalid.

The remaining two lines (three lines after discontinuation of the chemical measurements in 2006) of the 30 L min^{-1} flow were not used and went directly from the flow splitter to the pump box.

For the aerosol optical property measurements, the 30 L min^{-1} of the sample flow was further warmed by a secondary heater when necessary to maintain the system's RH at less than 40 %. The average temperature downstream of the secondary heater was 22 ± 4 °C during site operation (20 ± 3, 20 ± 3, 23 ± 5, and 22 ± 3 °C in the winter, spring, summer, and fall, respectively). Downstream of the secondary heater, a switched impactor system provided size-segregated measurements. The sample air first flowed through a Berner-type multi-jet cascade 10 μm impactor (∼ 7 μm aerodynamic diameter; Berner et al., 1979). An electronic ball valve was used to switch between a direct sample line to the instruments and a second Berner-type impactor with a size cut of 1 μm (∼ 0.7 μm aerodynamic diameter). Here, the 10 μm size cut is referred to as the total size cut or PM_{10}, while the 1 μm size cut is referred to as the submicron size cut or PM_1. Switching between PM_{10} and PM_1 size cuts

occurred every 6 min between April 2002 and May 2004, every 30 min between May 2004 and March 2006 to optimize humidograph operations, and then back to switching every 6 min after the humidograph was removed until the station closed in June 2017.

2.2 Aerosol chemical composition

For the first 4 years of measurements at the site, an additional 30 L min^{-1} of the flow from the flow splitter was pulled through a filter carousel system used to collect aerosol on filters for chemical analysis. The filter carousel system used the same PM_{10} and PM_1 impactors as the aerosol optical system. Results from an identical system were described in Quinn et al. (2002). The filters were analyzed by the Pacific Marine Environmental Laboratory (PMEL). More details of their analysis can be found in Quinn et al. (2000). The samples were analyzed using ion chromatography for major ionic species, including SO_4^{2-}, NH_4^+, Cl^-, Br^-, Na^+, K^+, Ca^+, Mg^+, NO^{3-}, methanesulfonic acid (MSA^-), and oxalate. Aerosol mass concentrations for both PM_1 (daily)
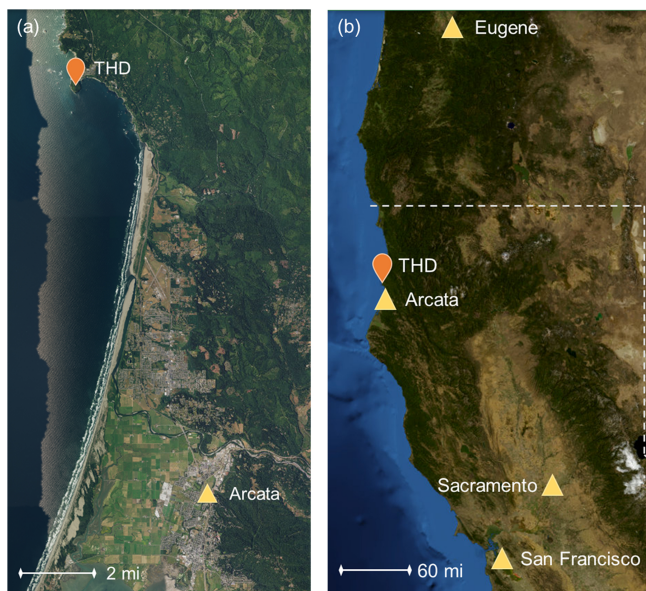
Figure 1. Maps of the measurement site in relation to major cities. A smaller scale is shown in panel **(a)** of the more local coastline, and a larger scale in panel **(b)** shows the broader area. Maps were constructed using images and information from the United States Geological Survey's program of The National Map (U.S. Geological Survey, 2019).

and for PM between $1\,\mu m < D_p < 10\,\mu m$ (weekly) were obtained. The PM_1 data were then averaged over the weekly sampling time of the 1–10 µm PM samples, and the two masses were added together to achieve a PM_{10} mass that could be compared to the optical data. It is important to note that some fraction of the NO^{3-} mass may have been driven off through the heating of the sampled air described above and, therefore, could be underestimated in this work (Bergin et al., 1997). For the first ~ 1.5 years of the program, local contamination episodes were identified when the wind was from the eastern and southeastern sectors (specifically 56–186°) and the chemical filtering system was bypassed. In addition to the wind direction, the particle number concentration (N) was used to identify periods of local contamination ($N > 8000\,cm^{-3}$; Sheridan et al., 2016). Chemical sampling was switched off during contamination periods. Identification of contamination using wind sector was stopped on 7 October 2003. It was determined that the airflow around the site was heavily influenced by the local topography and was leading to the elimination of non-contaminated data. Ion concentrations were compared to elemental measurements made with a rotating drum impactor that operated at THD during the spring of 2002 (Sect. S1 in the Supplement). Additionally, simple outlier testing was done on the filter data with monthly and seasonal analysis based on the interquartile range (IQR). Data points were defined as outliers and were not included in analysis if they fell outside the range

of $Q25 - (IQR \times 1.5)$ to $Q75 + (IQR \times 1.5)$, where $Q25$ and $Q75$ represent the 25th and 75th percentiles.

Contributions of non-sea-salt (nss) ion concentrations were calculated following the relationships outlined by Virkkula et al. (2006):

$$\text{Sea salt} = Cl^- + 1.47\,(Na^+) \tag{1}$$

$$\text{nss } SO_4 = SO_4^{2-} - 0.25\,(Na^+) \tag{2}$$

$$\text{nss } K = K^+ - 0.038\,(Na^+) \tag{3}$$

$$\text{nss } Mg = Mg^{2+} - 0.12\,(Na^+) \tag{4}$$

$$\text{nss } Ca = Ca^{2+} - 0.036\,(Na^+). \tag{5}$$

These relationships are based on the typical major ion concentrations in seawater. As these are calculated values, there are the possibilities for negative values in ion concentrations, and instances of this have been highlighted below.

2.3 Aerosol number concentration

A butanol-based condensation nuclei (CN) counter (model 3760, TSI Incorporated, Shoreview, MN, USA) was used to measure the number concentration of particles with diameter $> 0.14\,\mu m$. Between April 2002 and November 2005, the CN inlet was a separate 1/4 in. (0.635 cm) stainless-steel sample line that ran from the top of the 10 m stack directly to the instrument. The flow in this line was $\sim 10\,L\,min^{-1}$, where $1\,L\,min^{-1}$ was the CN sample flow and the remaining $9\,L\,min^{-1}$ were used for the counterflow Nafion drier to remove water vapor from the sample line. This was critical because water vapor is soluble in butanol and because as the butanol picks up water, the measurement quality degrades. In 2005, the CN sample line was changed to pick off the flow directly from the optical measurement line upstream of the secondary heater and impactor box.

2.4 Absorption and scattering measurements

Optical measurements consisted of aerosol absorption coefficients, measured by two different particle soot absorption photometers (PSAPs; Radiance Research; 1 wavelength or 3 wavelengths) or a continuous light absorption photometer (CLAP; NOAA; Ogren et al., 2017), in addition to aerosol total and back scattering coefficients, which were measured by an integrating nephelometer (model 3563; TSI Incorporated; Table 1). The aerosol absorption instruments were active during different times over the course of the 15-year measurement period. No overlap measurements exist for the 1- and 3-wavelength PSAPs in the field; however, a comparison between the 3-wavelength PSAP and CLAP absorption measurements during their overlap period at THD showed a high level of agreement (slope = 1.06 and $R^2 = 0.98$; Ogren et al., 2017). The CLAP sampled from the nephelometer blower block, as described in Ogren et al. (2017), while both PSAPs sampled from a pick-off ahead of the nephelometer inlet. All

three absorption instruments were operated at a flow rate of 1 slpm (standard liter per minute). Filter spot sizes for the three instruments are comparable, and so this consistent flow ensured similar face velocities and minimized potential discrepancies due to differences in particle penetration depths (Müller et al., 2011). All absorption measurements were corrected using the scheme reported by Bond et al. (1999) for the sample area, flow rate, and non-idealities in the manufacturer's calibration. Additionally, for the 3-wavelength absorption instruments, the method outlined by Ogren (2010) was used to correct the spectral absorption measurements. RH within the PSAP and CLAP instruments was not measured; however, the PSAP had an aftermarket heater (installed in October 2009), and the CLAP was maintained at 39 °C to minimize RH effects on the filter (Ogren et al., 2017).

The bulk of the $30 \, \text{L} \, \text{min}^{-1}$ sample flow exiting the switched impactors was sampled by an integrating nephelometer. The TSI nephelometer operates at wavelengths of 450, 550, and 700 nm, over an angular range of 7–170° (total scatter) and 90–170° (backscatter). The nephelometer scattering measurements were corrected for angular truncation and other instrument non-idealities, using the method described by Anderson and Ogren (1998). The PM_1 and PM_{10} nephelometer data were corrected using the Anderson and Ogren (1998) submicron and total corrections, respectively (see their Table 4). An insulating jacket was installed on the nephelometer in December 2012 to help lower the RH inside the instrument, which was monitored through an internal sensor.

2.5 Calculated parameters from optical measurements

Aerosol optical parameters were calculated from the measurements of spectral aerosol scattering and absorption coefficients (Table 2). These parameters are often used to provide insight into the characteristics of the aerosol such as size and composition. For example, Collaud Coen et al. (2007) described how the backscattering fraction (BFR) and scattering Ångström exponent (SAE) are sensitive to different parts of the aerosol size distribution, while Schmeisser et al. (2017) showed how the relationship between SAE and the absorption Ångström exponent (AAE) can act as a proxy for the composition of the aerosol. Both SAE and AAE were calculated using wavelength pairs rather than fitting across all three wavelengths. For SAE, the blue and green wavelengths (i.e., 450 and 550 nm) were used, as there have been some reported issues for the red scattering measured by TSI nephelometers (Collaud Coen et al., 2020). For AAE, the blue and red wavelengths (i.e., 450 and 700 nm) were used. These wavelengths were adjusted from the native wavelengths of the PSAPs and CLAP to match the wavelengths used by the nephelometer (Table 1).

In addition, an effective black carbon mass concentration (M_{eBC}) was calculated from the PSAP's measured absorption coefficient (σ_{ap}). This is referred to as an effective mass concentration because its calculation requires the assumptions that (1) all of the measured absorption is from black carbon and (2) all black carbon particles have uniform light absorption efficiencies. This calculation also requires assuming a value for the mass absorption cross section (MAC); frequently, $10 \, \text{m}^2 \, \text{g}^{-1}$ is used. Bond and Bergstrom (2006) suggest that a MAC of $10 \, \text{m}^2 \, \text{g}^{-1}$ is too high for freshly emitted light absorbing carbon, and through the synthesis of available measurements, they suggest an average MAC value of $7.5 \pm 1.2 \, \text{m}^2 \, \text{g}^{-1}$ for these aerosols. However, Bond and Bergstrom (2006) acknowledge that ambient and aged aerosol may have larger MAC values. For this work, the MAC of $10 \, \text{m}^2 \, \text{g}^{-1}$ was used, while recognizing that this could be an overestimate.

2.6 Positive matrix factorization analysis

To identify source groupings and contributions at THD, positive matrix factorization (PMF) was used through a consideration of the measured ion component masses and the calculated M_{eBC}. This study used PMF 5.0, as provided by the United States Environmental Protection Agency (Norris et al., 2014). PMF is a multivariate factor analysis method based on a weighted least squares fit, which was first developed by Paatero and Tapper (1993). The method is a receptor model which solves the chemical mass balance between measured species and source profiles, as shown in the equation below (Norris et al., 2014):

$$x_{ij} = \sum_{k=1}^{p} g_{ik} f_{kj} + e_{ij}, \qquad (14)$$

where x_{ij} is the concentration of available species (i is the sample number and j is the number of species), p is the number of factors believed to contribute to the concentrations, g_{ik} is the relative contribution of the kth factor to the ith sample, f_{kj} is the concentration of the jth species in the kth factor, and e_{ij} is the residual value for the jth species.

PMF operates under the constraint that none of the samples can have significantly negative source contributions and derives factor contributions and profiles by minimizing the objective function Q as follows (Paatero and Tapper, 1994; Paatero, 1997):

$$Q = \sum_{i=1}^{n} \sum_{j=1}^{m} \left[\frac{(x_{ij} - \sum_{k=1}^{p} g_{ik} f_{kj})}{u_{ij}} \right]^2. \qquad (15)$$

Here u_{ij} is the associated uncertainty for the sample x_{ij}. The associated errors for ion masses were calculated based on the uncertainty analysis provided by Quinn et al. (2000). Any species that were marked as weak in the analysis had an additional 3 % error applied. Since there was a large fraction of

Table 2. Derived aerosol optical properties using measured scattering and absorption coefficients.

Parameter (symbol)	Equation	Eq. no.	Instrument(s) used
Single-scattering albedo (SSA)*	$SSA = \frac{\sigma_{sp}}{\sigma_{sp}+\sigma_{ap}}$	(6)	Nephelometer and PSAP or CLAP
Scattering Ångström exponent (SAE)*	$SAE = -\frac{\log\sigma_{sp}(\lambda_1)-\log\sigma_{sp}(\lambda_2)}{\log\lambda_1-\log\lambda_2}$	(7)	Nephelometer
Absorption Ångström exponent (AAE)*	$AAE = -\frac{\log\sigma_{ap}(\lambda_1)-\log\sigma_{ap}(\lambda_2)}{\log\lambda_1-\log\lambda_2}$	(8)	PSAP or CLAP
Backscattering fraction (BFR)*	$b = \frac{\sigma_{bsp}}{\sigma_{sp}}$	(9)	Nephelometer
Asymmetry parameter (g)*	$g = -7.143889(BFR^3) + 7.464439(BFR^2)$ $-3.96356(BFR) + 0.9893$	(10)	Nephelometer
Submicron scattering fraction (R_{sp})*	$R_{sp} = \frac{\sigma_{sp,PM_1}}{\sigma_{sp,PM_{10}}}$	(11)	Nephelometer
Submicron absorption fraction (R_{ap})*	$R_{ap} = \frac{\sigma_{ap,PM_1}}{\sigma_{ap,PM_{10}}}$	(12)	PSAP or CLAP
Effective black carbon mass (eBC)	$M_{eBC} = \frac{\sigma_{ap}}{MAC}$	(13)	PSAP or CLAP

* In this work SSA, BFR, R_{sp}, and R_{ap} parameters were derived for the 550 nm wavelength. The SAE was derived using the 450 and 550 nm wavelength data, and the AAE was derived using the 450 and 700 nm wavelength data.

unidentified mass in the filter samples (Sect. 3.1.1), the sum of the identified ion mass and not PM_1 was used as the independent variable and total mass in the PMF model in order to avoid overestimating the factor contributions. The associated error for this mass was derived through the propagation of the individual ion errors.

Three error estimation methods were used to validate the PMF solutions, namely displacement analysis (DISP), bootstrap method (BS), and a combination of the two (BS–DISP). PMF solutions were only accepted and reported (1) if the observed drop in Q for DISP was below 0.1 % and no factor swaps occurred for $dQ_{max} = 4$, (2) from 100 bootstrap runs if all factors had a mapping of ≥ 90 %, and (3) if the observed drop in Q for BS–DISP was below 0.5 % (Brown et al., 2015; Paatero et al., 2014).

2.7　Humidograph measurements

From April 2002–March 2006, a scanning humidity conditioning system (Sheridan et al., 2001) and second nephelometer were operated in series with the first nephelometer in order to determine the scattering enhancement factor $f(RH)$ as a function of relative humidity (RH). The aerosol exited the first nephelometer, which was operating at low RH (so-called "dry") conditions into a humidity conditioner and controller that stepped the sample airstream through a humidity scan (humidities optimally ranged from ~ 40 % to ~ 90 %) over the course of an hour. The humidified airstream then entered the second "wet" nephelometer, and measurements of total scattering ($\sigma_{sp,wet}$) and backscattering coefficients ($\sigma_{sp,wet}$) as a function of relative humidity were obtained. The humidigraph generated hourly scans of increas-

ing RH, with alternating size cuts every 6 min between April 2002 and May 2004. From May 2004 to March 2006, the humidograph performed a 30 min increasing RH scan on the PM_{10} size cut and then 30 min decreasing RH scan on the PM_1 size cut, as this allowed better control at the high- and low-RH conditions. The scattering enhancement parameter at RH = 85 % and 550 nm was derived from fitting an equation of the following form:

$$f(RH,\lambda) = \frac{\sigma_{sp}(RH,\lambda)}{\sigma_{sp}(RH_{dry},\lambda)}. \tag{16}$$

We used the THD $f(RH)$ dataset (Burgos et al., 2019b), and further details about the data processing to calculate $f(RH)$ are described in the original publication (Burgos et al., 2019a). The value of $f(RH)$ presented here is the fitted value for wet scattering at 85 % and dry scattering measured at the RH of the dry nephelometer (Table 2). The dry nephelometer RH ranged from ~ 20 % in the winter to ~ 40 % in the summer, with an annual median dry nephelometer RH value of 29 %.

2.8　Meteorology

From 2002–2007 the only meteorological parameters measured were wind direction (WD) and wind speed (WS) at 10 m. In 2007, a suite of meteorological measurements was added to the site, including ambient temperature at 2 and 10 m, relative humidity at 2 m, and pressure at 2 m, as well as an additional anemometer for wind direction and speed at 10 m. A 4-year period of overlapping 10 m WD and WS measurements indicated good agreement between the original and new anemometer, and the original anemometer was

removed in 2011. Unfortunately, the RH measurements initiated in 2007 were determined to be invalid between 2007–2012 due to the problematic wiring of the sensor, so valid ambient RH data are only available for 2013–2017.

Typical wind directions were the same in summer and winter, but summer tended to be more influenced by flow from the ocean (the northwest). In contrast, in the winter, the wind was more likely to come from the land to the south and east of the site. The diurnal flow regimes indicated in Fig. S3 are consistent with typical onshore–offshore flow observed at many coastal sites. The southeasterly airflow pattern is a land breeze (flowing from land to ocean); it occurs primarily at nighttime (20:00–8:00 PST) and is directionally consistent with the air coming from nearby coastal communities and the local harbors. In contrast, the northwesterly flow occurs during the day, with the wind coming primarily from the Pacific Ocean. The wind rarely comes from the northeastern sector or the southwestern sector. It should be noted that due to the complex topography near the site, the local wind direction likely represents very local flow patterns. Monthly and diurnal statistical plots of wind data are included in the Supplement (Sect. S2).

3 Results and discussion

3.1 Aerosol chemical components

3.1.1 Seasonal cycles of ionic components

Seasonal median PM_{10} concentrations for 2002 to 2006 suggest that the ions most likely to be associated with sea salt (i.e., Na^+, Cl^-, Mg^{2+}, Ca^{2+}, K^+, and Br^-) are lower in the July–September time period and higher November through April (Fig. 2). This may be due in part to the lower wind speeds in the summer generating less sea spray. PM_1 ions whose primary source is likely to be sea salt (Na^+, Cl^-, Mg^{2+}, and Ca^{2+}) exhibit broadly similar seasonal cycles to those observed for the PM_{10} measurements, but there are differences in PM_1 and PM_{10} seasonality for other ions (Fig. 2). PM_{10} ions associated with marine biogenic activity (MSA^- and oxalate) peak in the summer. The PM_1 seasonal cycles for MSA^-, NH_4^+, and SO_4^{2-} are similar and peak in May–September, presumably due to marine biogenic activity. However, PM_1 oxalate exhibits relatively stable concentrations throughout the year. This indicates that PM_1 oxalate may come from multiple sources at different times, including biogenic, combustion, and anthropogenic sources (Rinaldi et al., 2011; Saarnio et al., 2010; Andreae, 1983; Baudet et al., 1990; Gao et al., 2003). PM_1 total mass, NO^{3-}, and K^+ concentrations peak in the cooler months (October–January) suggesting that these are likely related to anthropogenic activity (i.e., wintertime residential heating). Comparisons between the PM_{10} and PM_1 ion concentrations show that MSA^-, NH_4^+, SO_4^{2-}, and oxalate occur primarily in the PM_1 size range; their concentrations are often extremely

close to the median PM_{10} ion concentrations. Other measured ions, such as, Na^+, Cl^-, Mg^{2+}, and NO^{3-} are primarily in the supermicron size range; the PM_{10} concentrations of these ions are at least an order of magnitude higher than their PM_1 concentrations, suggesting a link to sea salt.

For both size fractions, the undetermined mass (which could be organics, insoluble ions, etc.) makes up between 60 %–80 % of the total mass throughout the year (Tables S1 and S2). The estimated contribution of black carbon is discussed later (Sect. 3.1.3). There is no obvious seasonal cycle in the undetermined mass fraction; however, there is seasonality in the fractional contribution of different ions to total ion mass (Fig. 3). Sea salt ions (Na^+, Cl^-, Mg^{2+}, and Ca^{2+}) make up the majority of PM_{10} ion mass in all four seasons; however, they only dominate the PM_1 ion mass in the winter. In the spring, summer, and fall SO_4^{2-} make up the largest fraction of PM_1 ion mass. Both the PM_1 and PM_{10} ion mass fractions of MSA^- are highest in the summer when marine biogenic activity increases. PM_1 fractions of K^+, NO^{3-}, and oxalate are highest in the winter and lowest in the summer; however, the PM_{10} fraction of K^+ is relatively consistent across all seasons, and PM_{10} fractions of NO^{3-} and oxalate are highest in the summer and lowest in the winter.

Since THD is a marine site, the aerosol chemistry will exhibit a strong sea salt component. It is therefore useful to elucidate the contributions of non-sea salt (nss) ion concentrations relative to those derived from marine sources. The relationships (Eqs. 1–5) from Virkkula et al. (2006) were used to calculate concentrations of sea salt and non-sea salt (nss) ion concentrations, using Na^+ as the reference species (Sect. 2.2). The estimated seasonal cycle of total concentrations for sea salt and contributions of nss SO_4^{2-}, K^+, Mg^{2+}, and Ca^{2+} to the total measured concentrations for both PM_1 and PM_{10} are shown in Fig. 4. Sea salt (due to soluble ions) makes up approximately 30 % of the identified PM_{10} mass concentration throughout the year but only 5 %–14 % of the PM_1 mass concentration. The lowest sea salt contributions to PM_1 occur from May to September, with higher sea salt contributions during the rest of the year. Virtually all of the PM_{10} K^+, Mg^{2+}, and Ca^{2+} values are attributable to sea salt (by default, Na^+ and Cl^- are assumed to be solely due to sea salt). Interestingly, the PM_{10} SO_4^{2-} was largely attributable to sea salt in the colder months (November–April); however, from May to October, the nss SO_4^{2-} fraction dominated the PM_{10} SO_4^{2-} total concentration. This pattern is consistent with increased biogenic activity in the summer being a source of SO_4^{2-}. Similar to PM_{10}, PM_1 Mg^{2+} can be almost entirely attributed to sea salt. In contrast, PM_1, SO_4^{2-} and K^+ appear to be primarily nss in origin, while PM_1 Ca^{2+} is marginally attributable to both sea salt and nss sources.
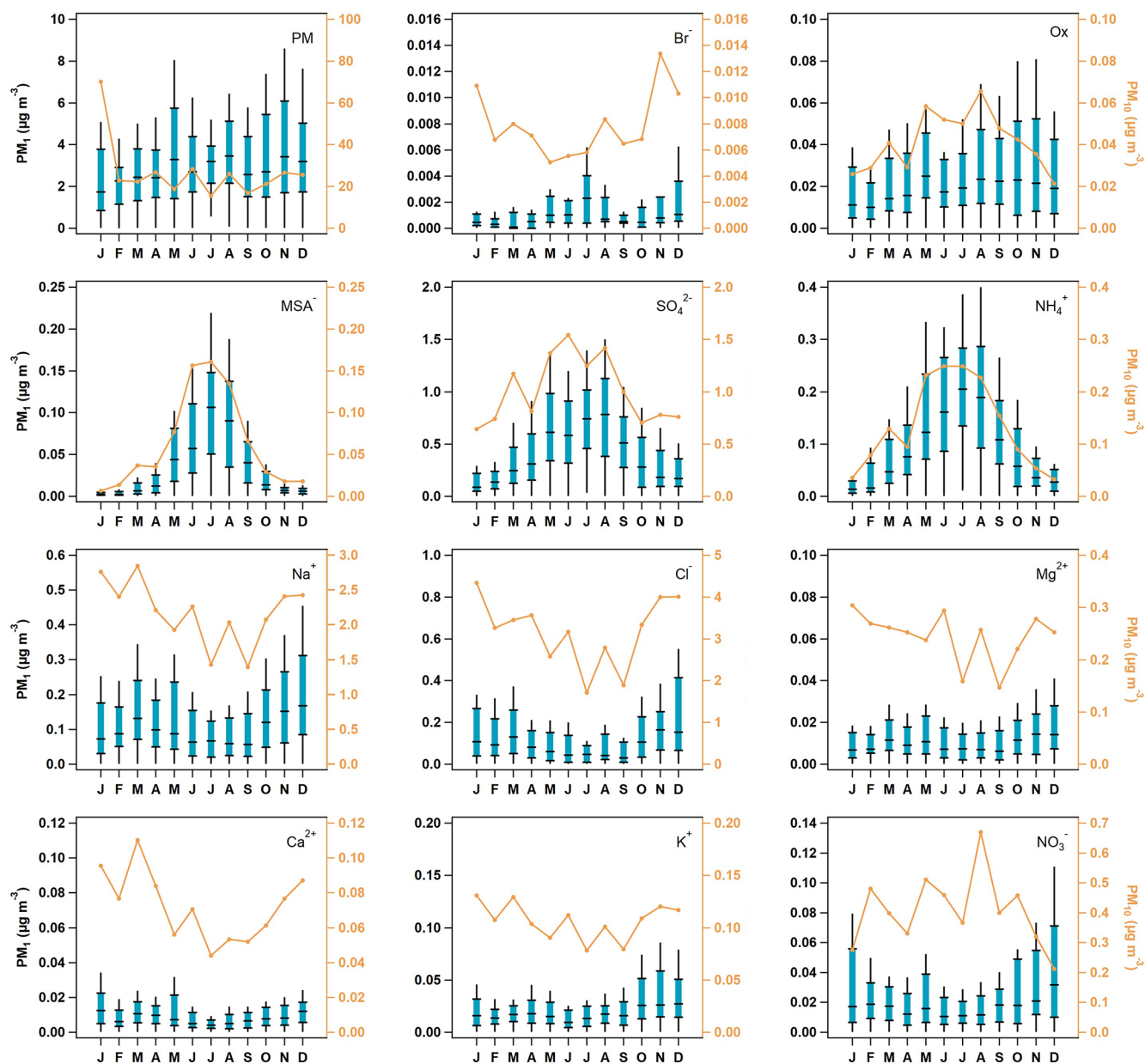
Figure 2. Seasonal aerosol mass and ion concentrations. The blue box-and-whisker plots represent PM_1 aerosol percentiles (5th, 25th, median, 75th, and 95th), and the orange line represents the median concentration of PM_{10} particles. The PM_1 data scale is on the left axis, while the PM_{10} is on the right, which has been color-matched to the PM_{10} trace.

3.1.2 Seasonal ionic relationships as source indicators

We further explored the seasonal relationships between all measured ions using a simple linear regression analysis. Following the ion mass fractions, in the winter, the PM_1 total mass has strong correlations ($r > 0.8$) with ions likely to be from sea salt (Na^+, Cl^-, Mg^{2+}, K^+, and Ca^{2+}), whereas in the summer, PM_1 has the strongest correlations with ions associated with biogenic activity (SO_4^{2-}, MSA^-, and oxalate). Sodium (Na^+), magnesium (Mg^{2+}), and chloride (Cl^-) are always highly correlated ($r > 0.8$), and all three ions have

significant relationships ($r > 0.5$) with calcium (Ca^{2+}) in all four seasons. Both Na^+ and Mg^{2+} correlate with potassium (K^+) in the winter, spring, and fall; however, Cl^- only has significant relationships with K^+ in the winter and fall. Sulfate (SO_4^{2-}) is always significantly correlated with methanesulfonic acid (MSA^-) and oxalate. However, MSA^- and oxalate only have strong linear relationships in the winter and summer. Additionally, SO_4^{2-} is highly correlated ($r > 0.9$) with ammonium (NH_4^+) in every season, indicating that particles in the area are largely composed of acidic compounds,
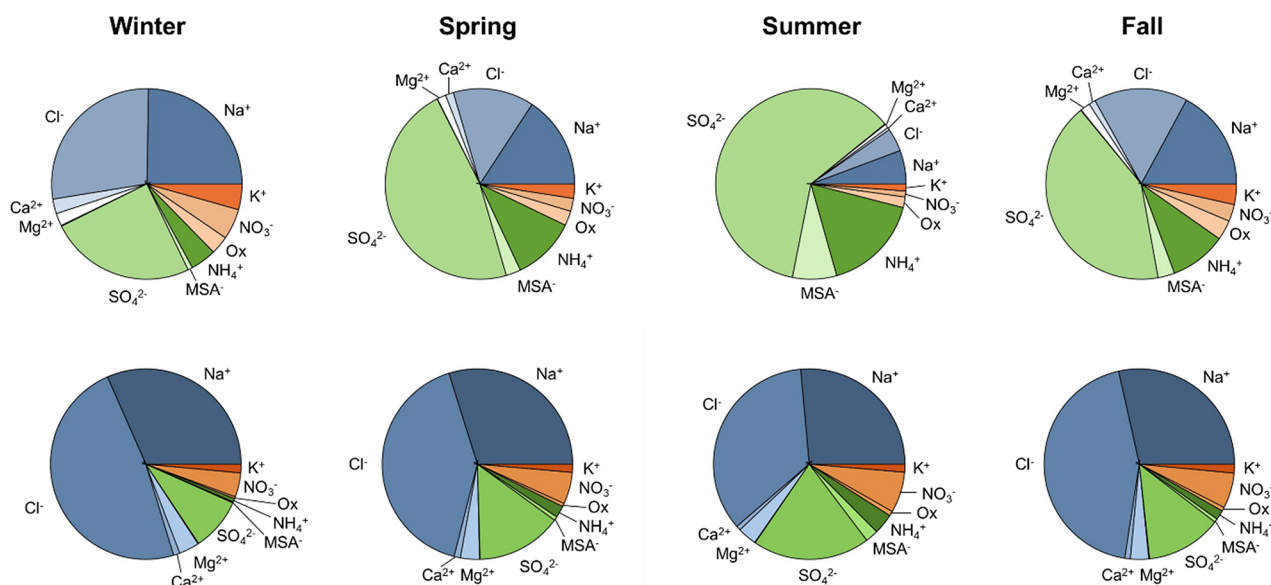
Figure 3. Ion mass fractions for PM_1 (top row) and PM_{10} (bottom row) in all four seasons. These data are based on total ion mass and not total PM_1 or PM_{10} mass. Undetermined mass is not included.

which is consistent with results presented by Allan et al. (2004), who observed a large particulate sulfate to ammonium ratio in the spring of 2002. Ions that are also associated with anthropogenic emissions (K^+, nitrate (NO^{3-}), and oxalate) are consistently correlated in the winter and fall. K^+ and oxalate also have a significant relationship in the spring, and the two ions both correlate with NO^{3-} in the summer. The correlation coefficients for all PM_1 ion relationships are listed in the Supplement (Table S3).

The PM_{10} data exhibit fewer significant relationships between ions, which could be the result of a reduced number of available data points due to weekly sampling. However, there are still clear relationships present. Just as with the PM_1 data, Na^+, Mg^{2+}, and Cl^- were always highly correlated ($r > 0.8$), and all three ions had significant relationships ($r > 0.5$) with Ca^{2+} in the spring, summer, and fall. Relationships between Na^+, Mg^{2+}, Cl^-, and K^+ were the most significant ($r > 0.8$) in the winter and fall. PM_{10} SO_4^{2-} is highly correlated ($r > 0.8$) with sea salt ions (Na^+, Cl^-, Mg^{2+}, and K^+) in the winter and in the other months is more consistently correlated with NH_4^+, NO^{3-}, MSA^-, and oxalate. This is consistent with our nss fraction analysis of SO_4^{2-}, which showed higher fractions of sea salt SO_4^{2-} in the winter months and lower fractions in other seasons. The correlation coefficients for all PM_{10} ion relationships are listed in the Supplement (Table S4).

From these relationships, there are clear seasonal source groupings of sea salt ions, biogenic ions, and anthropogenic ions. These patterns are further supported by changes in ion concentration ratios across seasons. For instance, the magnitude of the MSA^- to nss SO_4^{2-} mass concentration ratio can

be used to discriminate between the presence of clean marine air with enhanced biological activity when the ratio is high and the existence of anthropogenic sulfate when the ratio is low (Savoie and Prospero, 1989). The PM_1 MSA^- / nss SO_4^{2-} ratio at THD is highest in the summer, with median values ranging from 0.1–0.15 (equivalent to molar ratios of 8 %–12 %), and lowest in the winter, with median values of 0.02–0.03 that are nearly an order of magnitude lower than the summer ratios (Fig. S4). This generally agrees with the average PM_1 MSA^- / nss SO_4^{2-} ratio of 0.17 found by Millet et al. (2004) in the springtime period of the NOAA ITCT 2K2 study. Similarly, the mass concentration ratio of oxalate to nss SO_4^{2-} can provide evidence for clean marine air or air masses influenced by biomass burning. Zhou et al. (2017) reported oxalate-to-nss-SO_4^{2-} ratios of < 0.04 for clean air masses and ratios between 0.1–0.3 for biomass-burning-influenced air. At THD, the PM_1 oxalate / nss SO_4^{2-} ratio is lowest in the summer (0.03–0.04) and highest in the winter (0.1–0.15). This pattern is also observable in the PM_{10} ion ratios; however, there is larger variability (Fig. S4). These ratio values are further evidence of increases in biogenic sources at THD during the summer and increased influences from wood burning for home heating in the winter (City of Arcata, 2008).

3.1.3 Effective black carbon mass contribution

An effective black carbon mass concentration (M_{eBC}) was calculated for the data using the absorption coefficient (σ_{ap}) measured by the PSAP. Following the seasonal cycle in absorption (Sect. 3.2), M_{eBC} was highest in the colder months (September through February) and lowest in the summer
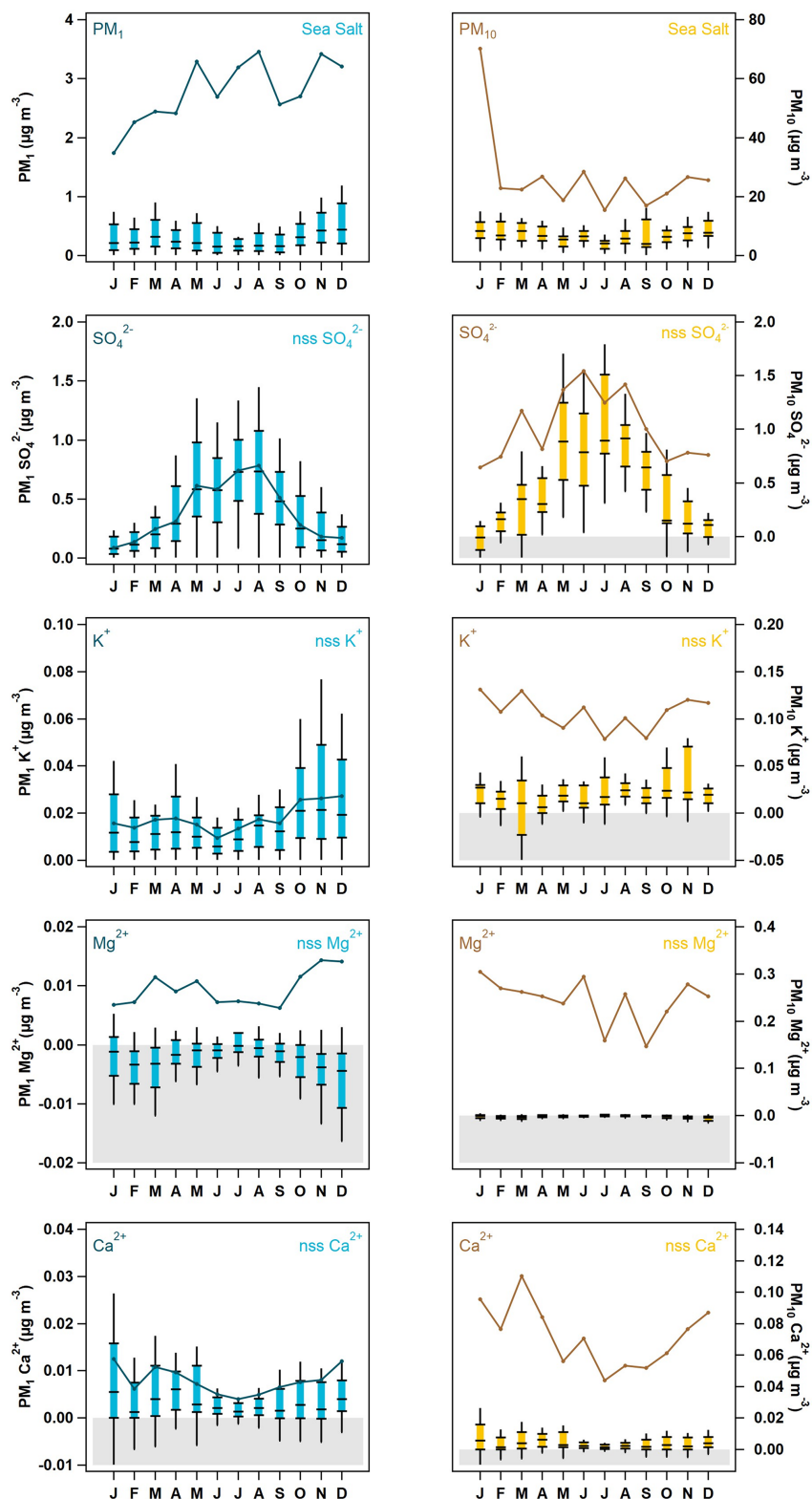
Figure 4. Seasonal cycle of PM_1 (blue) and PM_{10} (yellow) sea salt and ions with non-sea salt (nss) contributions. The box-and-whisker plots represent the sea salt and nss ion statistics (5th, 25th, median, 75th, and 95th percentiles), while the darker solid line shows the median total measured mass of the ion relative to the sea salt or nss component over the 4-year period. Concentrations that were calculated to be below zero are highlighted in gray in all plots.

(Fig. S6a). M_{eBC} also exhibited a distinct bimodal diurnal cycle (Fig. S6b), indicating regular sources in the mornings and evenings, which is likely from vehicular and/or maritime traffic. These seasonal observations are discussed further below (Sect. 3.2). For PM$_1$, M_{eBC} accounted for 1 %–2.5 % of the total mass, with larger fractions in the winter and fall (Table S1). In contrast, the contribution of M_{eBC} to PM$_{10}$ was negligible (> 0.5 %) in all seasons (Table S2).

A linear regression analysis of M_{eBC} against the other ions in both size fractions was done for the seasonal and monthly data. When grouped by season, PM$_1$ M_{eBC} only correlated with oxalate in the winter; however, segregating the data by month showed more relationships of interest. M_{eBC} correlated with PM$_1$, SO$_4^{2-}$, K$^+$, NO^{3-}, and oxalate in December and, surprisingly, also had a significant relationship with MSA$^-$ during this time. The correlations with SO$_4^{2-}$, K$^+$, and oxalate were also present in January, and other significant correlations appeared for K$^+$ and oxalate in other months (Table S5). For both SO$_4^{2-}$ and K$^+$, the correlation with M_{eBC} generally increased when only the non-sea-salt (nss) fraction of the ion concentrations was considered (Table S5). Similar patterns were observed in the PM$_{10}$ data (Table S6), with significant correlations between M_{eBC} and PM$_{10}$, SO$_4^{2-}$, K$^+$, NO^{3-}, MSA$^-$, and oxalate being most common in the October–February period. Winter and fall correlations with both SO$_4^{2-}$ and K$^+$ were again much improved when only the nss fractions were considered. These relationships provide further evidence for the presence of anthropogenic combustion sources in the winter and fall, which aligns with the ion seasonal cycles and correlations discussed previously.

3.1.4 Source identification using PMF analysis

To confirm the ionic source groupings indicated by the linear relationships described above, positive matrix factorization (PMF) was used (Norris et al., 2014). PMF analysis on the entire PM$_1$ ion dataset, without segregation by season, resulted in the identification of only two factors, based on the quality control criteria used (Sect. 2.3). However, separating the data by seasons resulted in a better resolution of source factors. It should be noted that this seasonal separation did lead to different weighting of ionic compounds among seasons, which is summarized in the Supplement, along with results of the PMF error analysis for each season (Sect. S4). Factor analysis (using an alternative method to the PMF analysis presented here) was performed previously by Millet et al. (2004) on hourly volatile organic compound (VOC) measurements collected at THD during the NOAA ITCT 2K2 study (19 April–22 May 2002). Within the higher-resolution ITCT springtime data, five factors were identified, namely (1) local anthropogenic emissions predominately from fossil fuel use, (2) oxygenated compounds from a variety of sources, (3) long-lived anthropogenic emissions, (4) compounds affected by local atmospheric mixing,

and (5) local terrestrial biogenic emissions. Both factors (1) and (4) were strongly influenced by local meteorology, indicating that loss of this resolution could be limiting our factor identification here. While PMF analysis was performed for each seasonal dataset, both the spring (March–May) and fall (September–November) data resulted in two-factor solutions that could not be validated based on subsequent error analysis and are therefore not included in the discussion here.

Good correlations were observed between the predicted and observed total identified ion mass for the winter ($y = 0.966x - 0.02$; $r^2 = 0.931$; Fig. S7a) and the summer ($y = 1.05x - 0.07$; $r^2 = 0.986$; Fig. S7b). For the winter (December–February), a three-factor solution was achieved (Fig. 5a). The first factor is determined to be sea salt, given the high contribution of Na$^+$, Mg^{2+}, and Cl$^-$. The second factor appears to be biogenic, with significant contributions from SO$_4^{2-}$, MSA$^-$, and NH$_4^+$, along with a small fraction of oxalate. Finally, the third factor is the anthropogenic combustion source, as shown by the high fractions of oxalate, K$^+$, and M_{eBC}. These factor profiles are consistent with the significant ion relationships identified in the winter. Additionally, the sea salt, biogenic, and anthropogenic–combustion factors were estimated to make up approximately 40 ± 30 %, 30 ± 20 %, and 30 ± 20 %, respectively, of the ion mass throughout the winter (Fig. 5a), which is fairly consistent with our direct ion mass calculations (Fig. 3). PMF analysis of the summer ion data (June–August) resulted in a two-factor solution (Fig. 5b). Similar to the winter, in the summer, the first factor is sea salt, with large contributions from Na$^+$, Ca^{2+}, and Mg^{2+}, while the second factor is biogenic, dominated by contributions from SO$_4^{2-}$, MSA$^-$, and NH$_4^+$ and a significant contribution from oxalate. Sea salt and biogenic factors made up approximately 40 ± 30 % and 60 ± 30 % of the ion mass in the summer, respectively. These factors are consistent with the summertime linear correlations and generally follow ion mass contributions (Fig. 3)

3.2 Aerosol optical properties

3.2.1 Seasonal cycles of optical properties

Seasonal cycles for the optical parameters are consistent across the 15 years of measurements, although the amount of aerosol (as indicated by scattering and absorption) decreases from the start to end of the measurements. General trends in aerosol optical properties at THD over time are further reported on by Collaud Coen et al. (2020). There is an obvious seasonality for most of the aerosol particle properties (Fig. 6), and the PM$_{10}$ aerosol exhibits similar seasonal patterns to those observed for the PM$_1$ data. The amount of aerosol – as represented by number concentrations (CN), light absorption, and light scattering (Fig. 6a, b, c) – is highest in fall and winter (September through January), with October and November having the highest aerosol loading and the summer months (June, July, and August) tend-
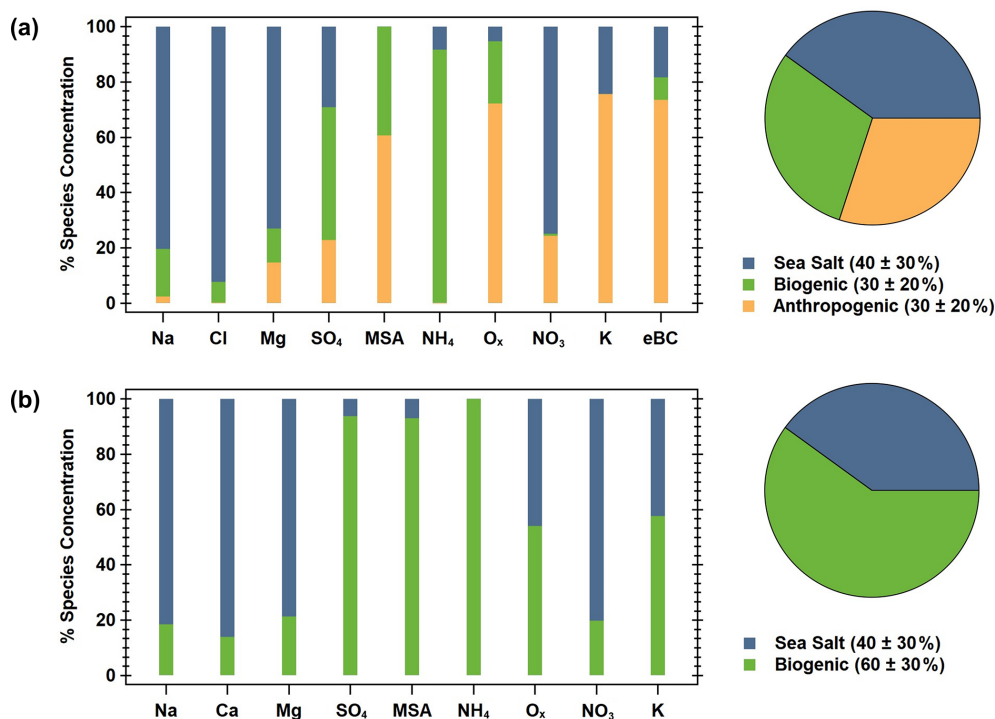
Figure 5. PMF factor information for the **(a)** winter and **(b)** summer. The bar charts show the ion species percent contribution to each factor (sea salt is blue, biogenic is green, and anthropogenic is orange), and the pie charts show the percent contribution (listed in the figure legends) of each factor to the seasonal PM_1 mass.

ing to have the lowest loading. The aerosol is darkest (i.e., single-scattering albedo (SSA) is lowest) in the fall and winter (Fig. 6e). A similarly timed decrease in SSA is noted at other (non-marine) North American sites, where it is attributed to less production and/or a more efficient removal of large, highly scattering particles during early autumn (Sherman et al., 2015).

The seasonality of the aerosol size distribution at THD can be indirectly observed through the monthly cycles in the scattering Ångström exponent (SAE), submicron scattering fraction (R_{sp}), and the backscatter fraction (BFR). The SAE (Fig. 6f) and submicron scattering fraction (R_{sp}; Fig. 6d) have similar seasonal patterns. Both SAE and R_{sp} are highest in summer, indicating a larger contribution from PM_1 particles, and lowest in the winter, demonstrating an increase in large particles. The median values of PM_{10} SAE (calculated from the 550 and 700 nm wavelength pair) at THD are always below 1.5, and the median values of R_{sp} are always below 0.6, indicating a significant contribution from supermicron aerosol (likely sea salt) throughout the year. BFR (Fig. 6i) exhibits the opposite pattern of SAE and R_{sp}; it is lowest in summertime, suggesting a shift toward larger accumulation mode particles in the warmer months. BFR and SAE are sensitive to different parts of the aerosol size distribution (Collaud Coen et al., 2007), so the summertime shift to a higher PM_1 particle contribution (increased SAE)

in conjunction with more, larger accumulation-mode particles (decreased BFR) could suggest a narrowing of the size distribution rather than inconsistency in the measurements. In contrast, the lower SAE and higher BFR values in winter could suggest that the size distribution is broader during that time of year. These relationships could also be attributed to changes in the number or relative importance of different aerosol size modes, as multi-modal size distributions can complicate the interpretation of SAE values (Schuster et al., 2006).

Little variation in the submicron absorption fraction (R_{ap}; Fig. 6g) is observable throughout the year. R_{ap} values suggests 80%–90% of absorption is PM_1 aerosol. In contrast, the absorption Ångström exponent (AAE, as calculated from the 450 and 700 nm wavelength pair; Fig. 6h) exhibits a strong seasonal cycle, with the lowest values (AAE < 1) observed in summer while larger values (AAE $\geq$ 1.5) are found in winter. AAE values of less than one have been associated with large, non-absorbing particles (Schmeisser et al., 2017), which is consistent with the increased SSA values in the summer, indicating the presence of primarily scattering aerosol (e.g., sea salt). As noted above, PM_{10} SAE is always less than 1.5, and in general, values of SAE in the summer are elevated, which also supports the presence of smaller non-absorbing aerosols in the summer.
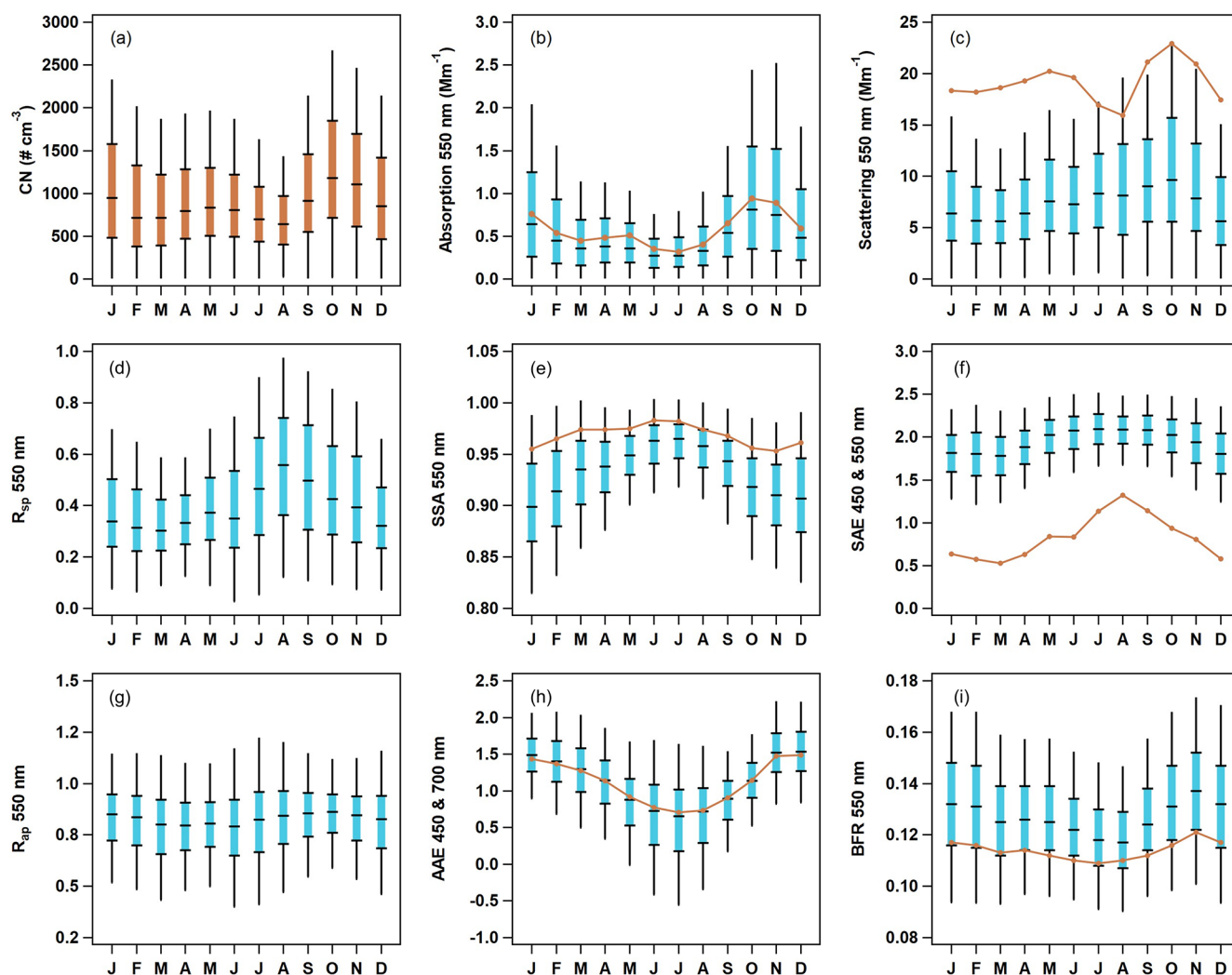
Figure 6. Seasonal cycles of aerosol optical properties at THD. The blue box-and-whisker plots represent PM_1 percentiles (5th, 25th, median, 75th and 95th), and the orange lines represent median values of PM_{10} optical data. Number concentration data **(a)** are also in orange, as they include both PM_1 and PM_{10}. The optical parameters presented are **(b)** absorption at 550 nm, **(c)** scattering at 550 nm, **(d)** submicron scattering fraction, **(e)** single-scattering albedo for 550 nm, **(f)** scattering Ångström exponent for 450 and 550 nm, **(g)** submicron absorption fraction, **(h)** absorption Ångström exponent for 450 and 700 nm, and **(i)** backscatter fraction at 550 nm.

3.2.2 Diurnal cycles of optical properties

Two different patterns are observable in the diurnal cycles of aerosol optical property data for all 15 years of sampling at THD (Fig. 7). The first pattern is bimodal, with peaks occurring at $\sim$ 09:00 and $\sim$ 21:00 PST. This pattern is most obvious for variables related to aerosol loading (i.e., CN concentration, absorption, and scattering; Fig. 7a, b, c) but is also seen in the diurnal cycles of the single-scattering albedo (SSA; Fig. 7e) and absorption Ångström exponent (AAE; Fig. 7h). The diurnal cycle for SSA has minima coinciding with the aerosol loading maxima. The timing of the diurnal SSA decrease and loading increase suggests a potential anthropogenic–combustion influence, likely vehicular and/or maritime traffic. This bimodal pattern occurs during all sea-

sons, although the timing of the peaks shifts slightly as a function of the season (not shown). The second pattern observed in the diurnal cycle plots is a single broad peak in the morning, with a maximum near 07:00 PST. This broad peak is seen in the plots depicting variables related to particle size (e.g., SAE, R_{sp}, and BFR; Fig. 7f, d, i). This suggests that smaller particles are most prominent in the early morning (06:00–08:00 PST), as indicated by increases in SAE, R_{sp}, and BFR at that time. Just like the bimodal cycles discussed earlier, there is some seasonal variation in the timing and amplitude of the broad peak (not shown). For most seasons, the peak occurs at a similar time in the morning, but in the summer, the amplitude of the broad peak is largest and occurs around noon (possibly related to marine biogenic activity).
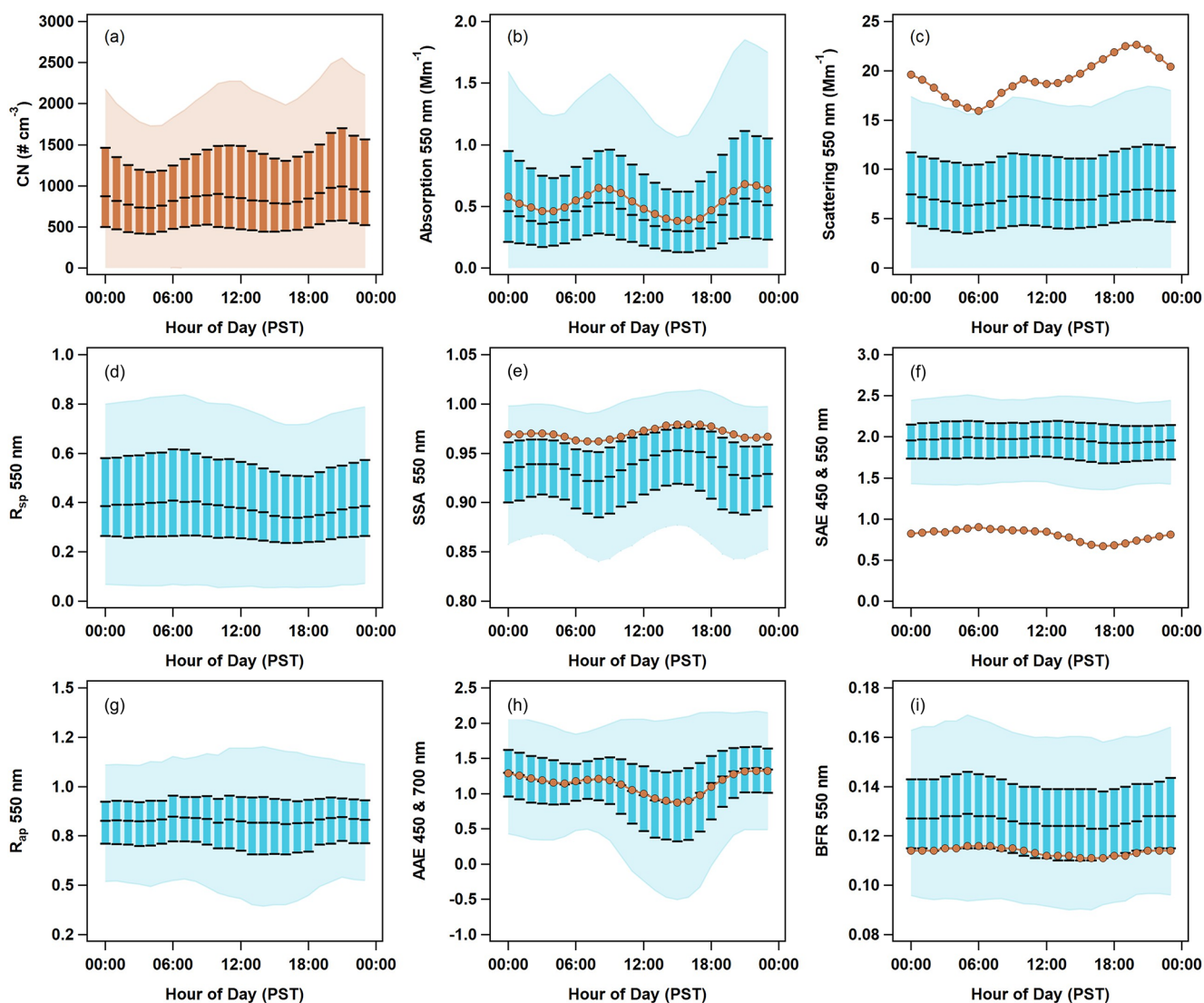
Figure 7. Diurnal cycles of aerosol optical properties at THD. Data are plotted against local time (Pacific standard time). PM_1 optical data are shown in blue, with the light blue shading representing the 5th to 95th percentile, and the blue boxes representing the interquartile range (25th to 75th percentile) and median. PM_{10} median values are shown as darker orange lines and markers. Number concentration data (**a**) are also in orange, as they include both PM_1 and PM_{10}. The optical parameters presented are (**b**) absorption at 550 nm, (**c**) scattering at 550 nm, (**d**) submicron scattering fraction, (**e**) single-scattering albedo for 550 nm, (**f**) scattering Ångström exponent for 450 and 550 nm, (**g**) submicron absorption fraction, (**h**) absorption Ångström exponent for 450 and 700 nm, and (**i**) backscatter fraction at 550 nm.

The submicron absorption fraction (R_{ap}; Fig. 7g) has negligible diurnal variability, suggesting little change in the sources of absorbing aerosol throughout the day.

3.2.3 Temporal cycles in $f(RH)$

Scattering enhancement parameters ($f(RH) = 85\%$) are relatively constant throughout the year with a value of ~ 2. In what follows $f(RH)$ will refer to the enhancement at $RH = 85\%$ unless otherwise stated. The PM_1 $f(RH)$ values are generally higher than those of the PM_{10} size cut. This is consistent with Zieger et al. (2010), who used Mie calcula-

tions to show that, for a given aerosol composition, $f(RH)$ will decrease as the mode diameter of the size distribution increases (their Fig. 9). This is due to the fact that the scattering efficiency factor (Q_{scat}) is more sensitive to changes in the particle size at smaller diameters where the Mie curve is steeper. At larger particle sizes, the Mie curve is relatively constant. Values for $f(RH)$ observed at THD are also consistent with the literature values of marine aerosol hygroscopicity synthesized in Titos et al. (2016).

Surprisingly, neither the average seasonal nor the diurnal cycles in the $f(RH)$ (Fig. 8a, b) reflect the changes in chemistry, particularly the higher levels of SO_4^{2-}, NH_4^+, and
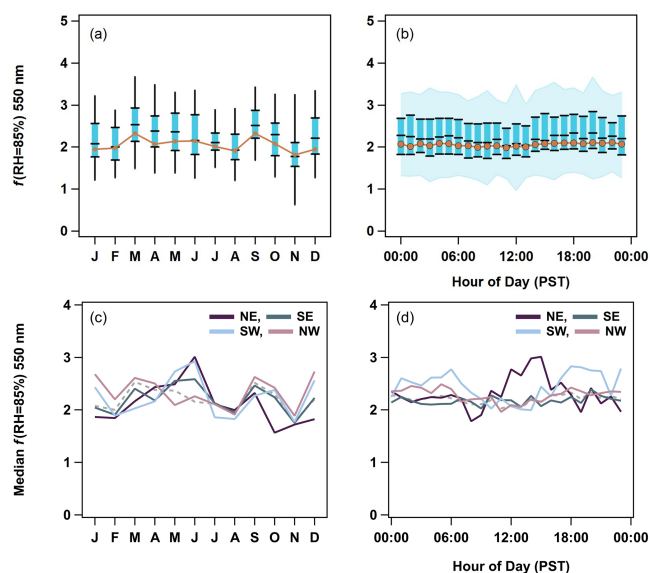
Figure 8. (a) Seasonal and **(b)** diurnal cycles of $f(\mathrm{RH})$ for 550 nm. The PM_1 5th to 95th percentiles are indicated by black lines in panel **(a)** and blue shading in panel **(b)**. The PM_1 25th to 75th interval is highlighted by blue boxes and black markers. Finally, PM_1 median values are black markers, and PM_{10} median values are the orange traces. The PM_1 $f(\mathrm{RH})$ cycles are then broken down by wind direction quadrants (northeast (NE), southeast (SE), southwest (SW), and northwest (NW)) on a **(c)** monthly and **(d)** hourly basis to show the changes in source regions. The median $f(\mathrm{RH})$ from all of the data is represented as a dashed gray trace in panels **(c)** and **(d)**.

MSA^- observed in the summer (Figs. 2, 3) and the local anthropogenic sources suggested by diurnal cycles in the optical properties (Fig. 7). Large fractions of sea salt could explain the stability in the PM_{10} $f(\mathrm{RH})$. This may also, in part, be due to the seasonal cycle of RH values in the dry nephelometer. Zieger et al. (2014) showed that marine aerosol may pick up significant amounts of water at RH values below 40 %. This could result in the seasonal cycle being masked due to the dry aerosol scattering not actually being dry at certain times of year. However, the prevalence of certain wind directions in the dataset clearly affects the overall seasonal cycles in $f(\mathrm{RH})$. Grouping the $f(\mathrm{RH})$ by four major wind quadrants – northeast (0–90°), southeast (90–180°), southwest (180–270°), and northwest (270–360°) – allows seasonal and diurnal cycles to emerge (Figs. 8c, d, S8, S9).

Both seasonal and diurnal cycles of PM_1 $f(\mathrm{RH})$ are weakest in the northwestern and southeastern quadrants, which dominated measurements at this site (Figs. S3, S8, S9). The northeastern sector shows patterns that indicate local anthropogenic influences, with $f(\mathrm{RH})$ being lowest in the fall and winter (October–February) and highest in the late spring and early summer (April–June). In the diurnal cycle, there is a decrease in $f(\mathrm{RH})$ at $\sim 08{:}00$ PST, after which the $f(\mathrm{RH})$ steadily increases until $\sim 16{:}00$ PST, which cor-

relates with patterns in the absorption coefficient and other optical properties (Fig. 7). This is evidence for an increase in hygroscopicity as fresh emissions from morning traffic age throughout the day, with the drop in $f(\mathrm{RH})$ later indicating the reintroduction of fresh combustion aerosols from afternoon traffic. These diurnal patterns are weaker but still present in the PM_{10} data (Figs. S9, S10). Further evidence of anthropogenic sources in the northeast are discussed later (Sect. 3.2.4). The southwestern quadrant has similar seasonal increase in $f(\mathrm{RH})$ in the late spring and early summer (April–June); however, this direction does not exhibit the same decrease in aerosol hygroscopicity in the fall and wintertime. In the diurnal cycle, $f(\mathrm{RH})$ is marginally higher before $\sim 07{:}00$ PST and after $\sim 17{:}00$ PST. This decrease in hygroscopicity could indicate continental influence during the day for winds from this sector; however, this is unlikely, as these decreases do not correlate with decreased SSA or increases in the scattering or absorption Ångström exponent values.

3.2.4 Wind sector analysis of optical properties and $f(\mathrm{RH})$

To elucidate the impact of different source regions, and subsequent seasonal changes in those sources, PM_{10} aerosol optical properties were binned both by wind direction and wind speed for summer and winter data (Fig. 9). This wind sector analysis could not be done with the ion mass concentration data because of insufficient time resolution in the data (PM_1 sampled on 24 h intervals and PM_{10} sampled over week-long periods), which would mask any wind-related information. However, possible changes in composition as a function of wind direction are supported by directional patterns in $f(\mathrm{RH})$ explored previously. Only data after 7 October 2003 were used in this analysis in order to ensure the consistent treatment of the data and remove periods in which wind-direction-based contamination screening process was applied (Sect. 2.2).

Significant differences between optical properties in the summer and winter are apparent in terms of magnitude, distribution across wind sectors, and relation to wind speed. Summertime aerosol number concentration and scattering exhibit more variability across wind directions and speeds but the patterns look quite similar to each other, suggesting a common source (Fig. 9a, e). Both number concentrations and scattering are high when the wind is from the north and relatively strong ($\sim 15\,\mathrm{m\,s^{-1}}$) and also when the wind is from the southeast and the wind speed is low ($< 5\,\mathrm{m\,s^{-1}}$). In the summer, absorption coefficients (Fig. 9c) are highest in air coming from the northeastern quadrant; this peak in absorption only occurs when wind speeds are low ($< 5\,\mathrm{m\,s^{-1}}$), suggesting a local source. In contrast, in the winter, number concentration and absorption cycles (Fig. 9a, c) look similar to each other and both exhibit the highest amount for low wind conditions (i.e., close to the center of each plot), suggest-
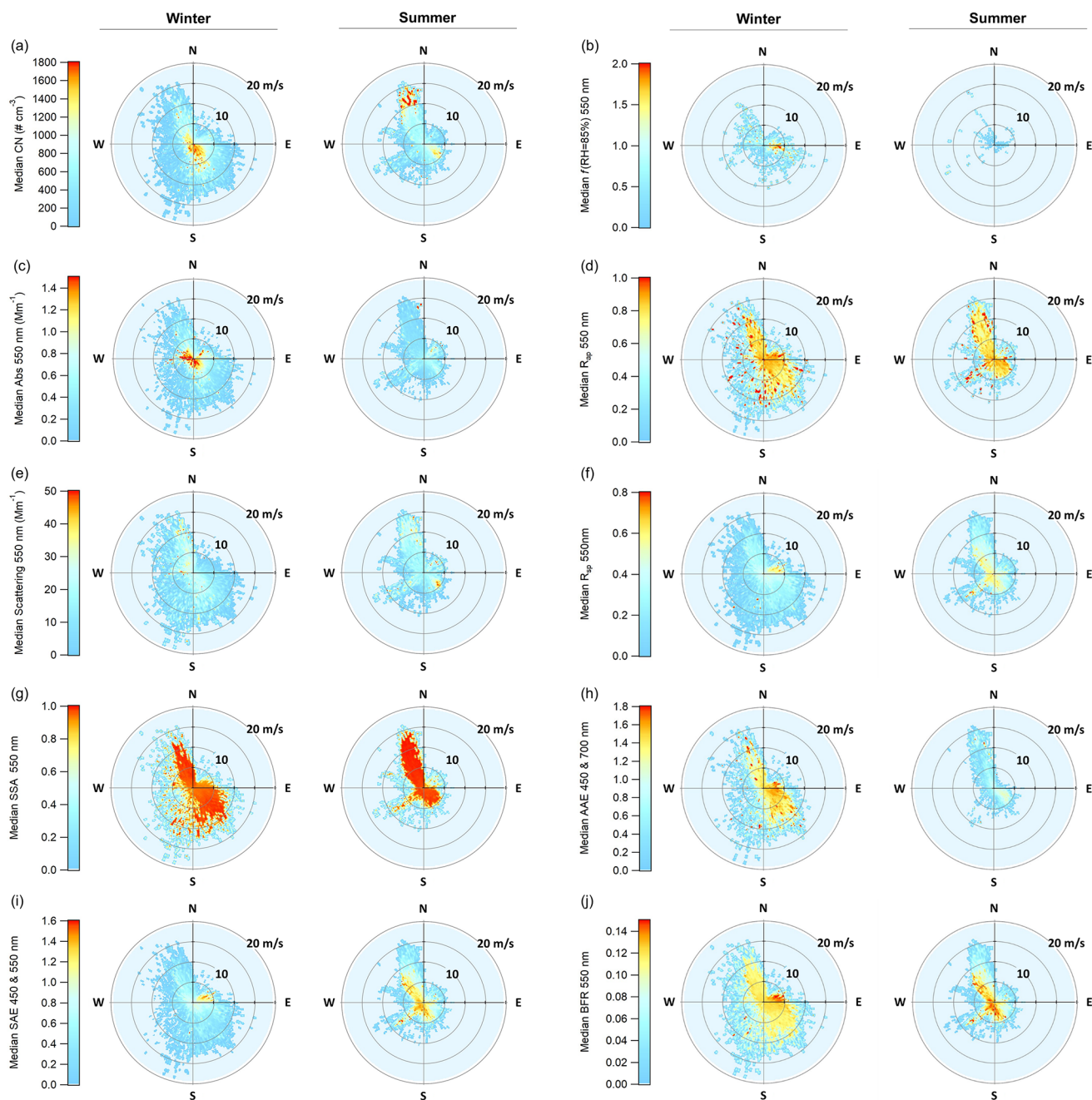
Figure 9. Wind vector analysis for PM_{10} aerosol optical properties and $f(RH = 85\%)$, showing the median value at a given wind speed and direction. For each property, the winter is on the left and the summer on the right. The color scale on the left applies to both figures.

ing more local influence and a common source. The highest wintertime scattering comes from the northwest, when wind speeds are high, suggesting increased wind-driven sea spray emissions (Fig. 9e).

Calculated optical properties provide more information about the characteristics of the aerosol in the different sectors. In the winter, there is a clear anthropogenic signal in the northeastern quadrant. Values of SSA are low, while SAE

and BFR are both high, suggesting smaller, darker aerosols such as those from combustion sources (Fig. 9g, i, j). This is likely related to home heating from wood burning (City of Arcata, 2008). The low wintertime SSA values correspond with low amounts of scattering in the northeastern quadrant (scattering values are less than $10\,Mm^{-1}$) and higher amounts of absorption, possibly due to preferential removal of scattering aerosol. Low SAE values also correspond with

the lowest observed $f(\mathrm{RH})$ (Fig. 9b), which is consistent with combustion-related aerosol (Maßling et al., 2003; Titos et al., 2016). In the summer, the scattering and the absorption in the northeastern sector both exhibit high values at low wind speeds, and the SSA in the quadrant is generally lower than for the other sectors, again suggesting some sort of local anthropogenic source in that direction. Finally, this temporal cycle is also supported by higher SAE values, indicating a larger contribution of submicron aerosol. It is important to recall that the winds at THD are relatively rare from the northeastern quadrant ($\sim 9\%$ overall; $\sim 7\%$ in summer and $\sim 14\%$ in winter; e.g., Fig. S3), so the overall contribution from the quadrant to the aerosol climatology is limited. This was observed previously in the climatology of $f(\mathrm{RH})$ values.

For both summer and winter, SAE values are lower at higher wind speeds ($> 10\,\mathrm{m\,s^{-1}}$), consistent with wind-driven emissions of sea spray (Vaishya et al., 2012). During the summer, the highest SAE values occur during southwesterly flow. This is potentially related to marine biogenic activity, as has been suggested in studies for other marine-influenced sites (Quinn et al., 2002; Yoon et al., 2007) and which is supported by the $f(\mathrm{RH})$ observations for the southwestern quadrant (Sect. 3.2.3). The link between AAE and marine air masses is not clearly defined. For example, Schmeisser et al. (2017) observed that though many of the marine air masses at the sites they studied tended towards lower AAE, no clear pattern could be characterized. The AAE at THD, although exhibiting different values over the seasons, shows a shift from higher AAE in the east (land) to lower AAE in the west (ocean), which generally suggests increased influence from clean marine air (Fig. 9h). This is expected, given the geography of THD.

The relationship between AAE and SAE is thought to be a possible indicator of the type of aerosol being measured (Cappa et al., 2016; Cazorla et al., 2013); however, these regimes have been shown to be less reliable at locations with complex conditions and source types (Schmeisser et al., 2017). In this work, we used the classification scheme from Cappa et al. (2016) to look at general regimes by separating AAE and SAE (450 and 700 nm) comparisons according to both wind direction and season, along with aerosol size, in order to more effectively classify the changes in aerosol types at THD (Fig. S11). PM_1 winter data were largely concentrated in the black carbon (BC)-dominated and BC / brown carbon mixture regions. This shifted down towards the small particle–low absorption region in the spring through fall, with the highest concentration of data in this region during the summer. In all four seasons, the data from the western and eastern quadrants were stratified, with higher ratios for easterly winds (45–135° consistently had the highest ratios of AAE to SAE). Along with the other evidence presented, this supports increased combustion sources in the winter and fall that mainly come from the east, with more biogenic activity in the summer from the west. Comparisons for the PM_{10} data were similar, although predictably shifted toward larger particle regimes. In contrast to the other seasons, the summer PM_{10} data from the west remained in the small particle–low absorption group and did not shift into the large particle–low absorption region. Higher R_{sp} values in the summer support this and point to the formation of small biogenic aerosol during the summer to the west of THD (Fig. 9f).

3.3 Patterns in aerosol composition and optical properties

Aerosol chemical and optical properties have been linked previously at other marine sites. For example, aerosol data from NOAA's Barrow Observatory (Utqiaġvik, AK, USA) exhibited a strong ($R^2 = 0.8$) correlation between $\mathrm{MSA^-}$ and CN concentration during the summer (Quinn et al., 2002), which they attributed to particle formation from biogenic sources. Quinn et al. (2002) also performed linear regressions of aerosol scattering versus derived sea salt and nss $\mathrm{SO_4^{2-}}$ concentrations at Barrow Observatory and found relatively strong positive correlations ($R^2 > 0.5$) for some seasons. At THD, a negligible number of significant relationships ($r > 0.5$) is observed between ion and CN concentrations; however, several relationships between ion chemistry, scattering, and absorption exist (Tables S9, S10, S11, and S12). Scattering coefficients (σ_{sp}) correlate with PM_1 mass in the winter and summer. In the summer, σ_{sp} has a significant relationship with $\mathrm{MSA^-}$ in July and in August but not in June, indicating the biogenic production of small scattering aerosols in those months. Interestingly, σ_{sp} correlates with both $\mathrm{K^+}$ and oxalate in the winter (σ_{sp} and $\mathrm{SO_4^{2-}}$ relationships are significant in December and close to significant in January), and the absorption coefficient (σ_{ap}) correlates with $\mathrm{SO_4^{2-}}$, $\mathrm{K^+}$, and oxalate only in the January data. These individual ion to optical relationships are consistent with the PMF analysis discussed previously (Sect. 3.1.4). The PM_1 anthropogenic–combustion factor correlates with the absorption coefficient, indicating that it is driving the increased absorption in the colder months (Fig. S12). While neither the sea salt nor biogenic factors had significant relationships with the scattering coefficient, the biogenic patterns were the stronger (larger r) of the two in both seasons, indicating a stronger impact on scattering (Fig. S12).

Another approach to looking at relationships between aerosol chemistry and optical properties is to segment the data by SSA (550 nm) and SAE (450 and 550 nm) and look for differences in mass concentrations for the different groupings of data. This segmentation was done for the PM_1 data (Fig. 10), using the 25th and 75th percentiles of SSA (0.89 and 0.95) and SAE (1.91 and 2.24). Five aerosol groups were defined using the following bounds: big-scattering (SSA > 0.95, SAE < 1.91), small-scattering (SSA > 0.95, SAE > 2.24), mixed (0.89 $<$ SSA $<$ 0.95, 1.91 $<$ SAE $<$ 2.25), small-absorbing (SSA < 0.89, SAE > 2.24), and big-absorbing (SSA < 0.89, SAE < 1.91) aerosols. These group classifica-
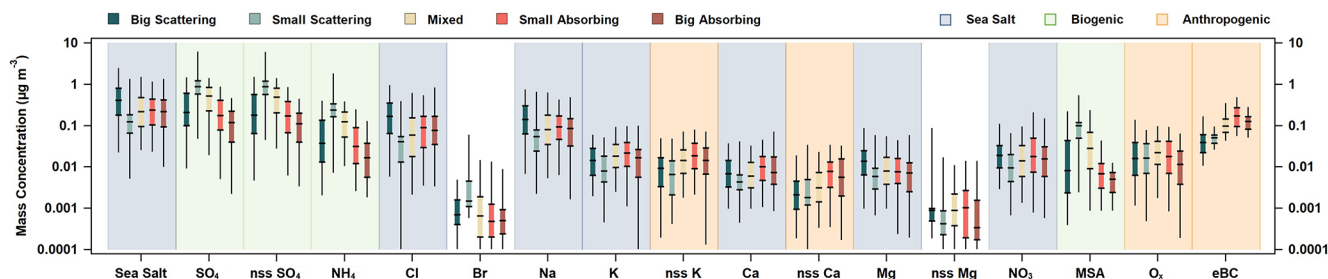
Figure 10. PM_1 ion mass concentrations, together with sea salt and M_{eBC}, as a function of SSA (550 nm) and SAE (450 and 550 nm). For each species, the mass of big-scattering (SSA > 0.95, SAE < 1.91), small-scattering (SSA > 0.95, SAE > 2.24), mixed (0.89 < SSA < 0.95, 1.91 < SAE < 2.25), small-absorbing (SSA < 0.89, SAE > 2.24), and big-absorbing (SSA < 0.89, SAE < 1.91) aerosol fractions are listed from left to right and color-coded, as outlined in the top-left legend. Additionally, one possible source of the ion based on its distribution across the aerosol types is indicated using shading. Blue shading indicates a sea-salt-related component, green indicates biogenic-related components, and orange indicates anthropogenic–combustion relationships (in the top-right legend).

tions are linked to common aerosol types, such as, marine (big scattering), secondary nucleation (small scattering), anthropogenic (small absorbing), and dust (big absorbing). Bigger, more scattering aerosols had higher concentrations associated with calculated sea salt and its associated ions (Cl^-, Na^+, and Mg^{2+}), while smaller, more scattering aerosols had higher concentrations of biogenic-related ions (MSA^-, SO_4^{2-} (total and nss fraction), and NH_4^+). For darker aerosols, the median for the small-absorbing mass concentration was larger than that of the big-absorbing mass concentration for every species investigated, except Br^-. Looking at the mass for each of these groups within a given species, patterns in source-related ions and chemical components can be observed (Figs. 10, S13).

3.4 THD as a representative marine site

THD was part of the NOAA Federated Aerosol Network (NFAN), which also includes several clean marine sites at Kennaook / Cape Grim (Australia), Cape Point (South Africa), Samoa (American Samoa), Cape San Juan (Puerto Rico), and Sable Island (Canada; Andrews et al., 2019). Data from these sites compared to that from polluted marine environments show a strong separation between aerosol optical properties (Table 3). Clean marine sites tend to meet the following criteria: $\sigma_{sp} < 40\,Mm^{-1}$, $\sigma_{ap} < 1\,Mm^{-1}$, SSA > 0.97, and SAE < 1. Anthropogenically impacted sites fail to meet one or more of these constraints. Diurnal variability at clean marine sites is minor, as shown by Delene and Ogren (2002), who reported virtually no diurnal variability in either SSA or BFR at Sable Island (1992–2000), suggesting minimal influence from local sources. THD has diurnal cycles suggestive of anthropogenic influences, similar to those observed by Bhugwant et al. (2001) for absorbing aerosol at a coastal site on Réunion island. However, looking at THD data as a whole, they align most closely with other clean marine sites (Table 3). Comparison to vertical profiles of absorption over the Pacific during the multi-year ATOM (Atmospheric To-

mography Mission) campaign can also clarify THD's status as a clean marine site. During ATOM the average mass mixing ratio of refractive black carbon (rBC) in the 20–60° N latitude range over the Pacific Ocean from ATOM was approximately $10\,ng\,kg^{-1}$ at the lowest flight level ($\sim 0.2\,km$), which is equivalent to an σ_{ap} of $\sim 1.2\,Mm^{-1}$ (assuming dry air mass density of $1.2\,kg\,m^{-3}$ and MAC $10\,m^2\,g^{-1}$; Katich et al., 2018). This is well within the range of the aerosol σ_{ap} measured at THD (Figs. 6, 7), with an annual median σ_{ap} of $0.62\,Mm^{-1}$. This leads to the conclusion that, even with influences from local vehicular and marine traffic, seasonal wood burning, and marine biogenic emissions, the majority of measurements made at THD are representative of clean marine air.

4 Conclusions: aerosol sources at THD and THD as a representative marine site

This paper presents the seasonal climatology of aerosol chemical and optical properties from a 15-year dataset obtained at NOAA's now-closed Trinidad Head observatory. As expected, sea salt aerosol is a consistent source at THD and was identified as a source factor in every season (Fig. 5). Calculated sea salt mass, and the mass of its associated ions, consistently dominates PM_{10} and contributes strongly to PM_1 in the winter (Figs. 2, 3). A consistent PM_{10} SAE of less than 1.5 and R_{sp} of less than 0.6 also show the influence of large non-absorbing sea salt throughout the year (Fig. 6). Over all seasons, SAE was lower, and the concentrations of sea salt ions increased at higher wind speeds, indicating wind-driven sea spray emissions that mainly come from the western (ocean-side) quadrants around THD (Fig. 9). Additionally, aerosols at THD are largely composed of acidic compounds, as demonstrated by the relationship between sulfate and ammonium ions in all seasons.

Table 3. In situ annual aerosol property statistics at long-term coastal monitoring sites (PM_{10} or no size cut). Values are reported at the green wavelength (at or near 550 nm) for scattering, absorption, and SSA, unless otherwise noted. Presented SAE values were calculated for a blue or green wavelength pair, unless otherwise indicated (*). Values are medians, unless the only available statistic was a mean value.

	Site	Scattering (Mm^{-1})	Absorption (Mm^{-1})	SSA	SAE
Clean Marine	THD	21.5	0.62	0.97	0.78
	Cape Point, South Africa[1]	18.8	0.26	0.98	0.43
	Samoa, American Samoa[1]	21.4	–	–	−0.16
	Mace Head, Ireland[2,3,4]	10–30	0.15–0.20	0.94–1.0	0.2–0.8*
	Cape San Juan, Puerto Rico[1]	29	0.75	0.97	0.35
	Sable Island, Canada[1]	34	0.66	0.98	0.75
	Average	24 ± 8	0.4 ± 0.3	0.97 ± 0.02	0.4 ± 0.4
Anthropogenically Influenced marine	El Arensosillo, Spain[1]	35.4	3.23	0.91	1.38
	Gulf of Cádiz, Spain[5]	38	–	–	1.47*
	Finokalia, Greece[6]	50	5.6	0.89	–
	Gosan, South Korea[1]	72.8	5.6	0.93	0.75
	Hok Tsui, Hong Kong SAR[7]	134	6.6	0.94	1.4*
	Anmyeondo, South Korea[1]	113.9	9.69	0.92	1.48
	Average	70 ± 40	6 ± 2	0.92 ± 0.02	1.2 ± 0.4

* SAE was measured for the blue and red wavelengths. [1] Andrews et al. (2019). [2] Vaishya et al. (2011). [3] O'Dowd et al. (2012). [4] Jennings et al. (2003). [5] López et al. (2015). [6] Vrekoussis et al. (2005). [7] Wang et al. (2017).

Aerosol ion chemistry and optical properties at THD exhibit monthly and diurnal temporal cycles, suggesting changes in sources, sinks, and transport throughout the year. Biogenic activity contributes to aerosol concentration throughout the year; however, the source is much stronger in the summer (Figs. 2, 3, 5, S4). Large contributions of these small scattering aerosols contribute to both PM_1 and PM_{10} the summer (Figs. 6, 10, S13). While daily cycles in aerosol optical properties indicate some influence from local traffic emissions (Fig. 7), the winter is the only season with a persistent anthropogenic–combustion source (Figs. 8, 9). This source is only identifiable in the winter (Figs. 5, S4) – likely from wood burning for home heating – and is the driver of increased absorption during this time (Figs. 6, S12). These sources could be further parsed into subcategories; however, this would require higher-resolution chemical data.

References

Allan, J. D., Bower, K. N., Coe, H., Boudries, H., Jayne, J. T., Canagaratna, M. R., Millet, D. B., Goldstein, A. H., Quinn, P. K., Weber, R. J., and Worsnop, D. R.: Submicron aerosol composition at Trinidad Head, California, during ITCT 2K2: Its relationship with gas phase volatile organic carbon and assessment of instrument performance, J. Geophys. Res.-Atmos., 109, D23S24, https://doi.org/10.1029/2003JD004208, 2004.

Anderson, T. L. and Ogren, J. A.: Determining Aerosol Radiative Properties Using the TSI 3563 Integrating Nephelometer, Aerosol Sci. Tech., 29, 57–69, https://doi.org/10.1080/02786829808965551, 1998.

Andreae, M. O.: Soot Carbon and Excess Fine Potassium: Long-Range Transport of Combustion-Derived Aerosols, Science, 220, 1148–1151, https://doi.org/10.1126/science.220.4602.1148, 1983.

Andreae, M. O.: Aerosols Before Pollution, Science, 315, 50–51, https://doi.org/10.1126/science.1136529, 2007.

Andrews, E., Sheridan, P. J., Ogren, J. A., Hageman, D., Jefferson, A., Wendell, J., Alástuey, A., Alados-Arboledas, L., Bergin, M., Ealo, M., Hallar, A. G., Hoffer, A., Kalapov, I., Keywood, M., Kim, J., Kim, S.-W., Kolonjari, F., Labuschagne, C., Lin, N.-H., Macdonald, A., Mayol-Bracero, O. L., McCubbin, I. B., Pandolfi, M., Reisen, F., Sharma, S., Sherman, J. P., Sorribas, M., and Sun, J.: Overview of the NOAA/ESRL Federated Aerosol Network, B. Am. Meteorol. Soc., 100, 123–135, https://doi.org/10.1175/BAMS-D-17-0175.1, 2019.

Bates, T. S., Huebert, B. J., Gras, J. L., Griffiths, F. B., and Durkee, P. A.: International Global Atmospheric Chemistry (IGAC) Project's First Aerosol Characterization Experiment (ACE 1): Overview, J. Geophys. Res.-Atmos., 103, 16297–16318, https://doi.org/10.1029/97JD03741, 1998.

Baudet, J. G. R., Lacaux, J. P., Bertrand, J. J., Desalmand, F., Servant, J., and Yoboué, V.: Presence of an atmospheric oxalate source in the intertropical zone – its potential action in the atmosphere, Atmos. Res., 25, 465–477, https://doi.org/10.1016/0169-8095(90)90029-C, 1990.

Bergin, M. H., Ogren, J. A., Schwartz, S. E., and McInnes, L. M.: Evaporation of Ammonium Nitrate Aerosol in a Heated Nephelometer: Implications for Field Measurements, Environmental Sci. Technol., 31, 2878–2883, https://doi.org/10.1021/es970089h, 1997.

Berner, A., Lürzer, C., Pohl, F., Preining, O., and Wagner, P.: The size distribution of the urban aerosol in Vienna, Sci. Total Environ., 13, 245–261, https://doi.org/10.1016/0048-9697(79)90105-0, 1979.

Bhugwant, C., Bessafi, M., Rivière, E., and Leveau, J.: Diurnal and seasonal variation of carbonaceous aerosols at a remote MBL site of La Réunion island, Atmos. Res., 57, 105–121, https://doi.org/10.1016/S0169-8095(01)00066-7, 2001.

Bond, T. C. and Bergstrom, R. W.: Light Absorption by Carbonaceous Particles: An Investigative Review, Aerosol Sci. Tech., 40, 27–67, https://doi.org/10.1080/02786820500421521, 2006.

Bond, T. C., Anderson, T. L., and Campbell, D.: Calibration and Intercomparison of Filter-Based Measurements of Visible Light Absorption by Aerosols, Aerosol Sci. Tech., 30, 582–600, https://doi.org/10.1080/027868299304435, 1999.

Brock, C. A., Cozic, J., Bahreini, R., Froyd, K. D., Middlebrook, A. M., McComiskey, A., Brioude, J., Cooper, O. R., Stohl, A., Aikin, K. C., de Gouw, J. A., Fahey, D. W., Ferrare, R. A., Gao, R.-S., Gore, W., Holloway, J. S., Hübler, G., Jefferson, A., Lack, D. A., Lance, S., Moore, R. H., Murphy, D. M., Nenes, A., Novelli, P. C., Nowak, J. B., Ogren, J. A., Peischl, J., Pierce, R. B., Pilewskie, P., Quinn, P. K., Ryerson, T. B., Schmidt, K. S., Schwarz, J. P., Sodemann, H., Spackman, J. R., Stark, H., Thomson, D. S., Thornberry, T., Veres, P., Watts, L. A., Warneke, C., and Wollny, A. G.: Characteristics, sources, and transport of aerosols measured in spring 2008 during the aerosol, radiation, and cloud processes affecting Arctic Climate (ARCPAC) Project, Atmos. Chem. Phys., 11, 2423–2453, https://doi.org/10.5194/acp-11-2423-2011, 2011.

Brown, S. G., Eberly, S., Paatero, P., and Norris, G. A.: Methods for estimating uncertainty in PMF solutions: Examples with ambient air and water quality data and guidance on reporting PMF results, Sci. Total Environ., 518–519, 626–635, https://doi.org/10.1016/j.scitotenv.2015.01.022, 2015.

Browse, J., Carslaw, K. S., Arnold, S. R., Pringle, K., and Boucher, O.: The scavenging processes controlling the seasonal cycle in Arctic sulphate and black carbon aerosol, Atmos. Chem. Phys., 12, 6775–6798, https://doi.org/10.5194/acp-12-6775-2012, 2012.

Brunke, E. G., Labuschagne, C., Parker, B., Scheel, H. E., and Whittlestone, S.: Baseline air mass selection at Cape Point, South Africa: application of 222Rn and other filter criteria to CO_2, Atmos. Environ., 38, 5693–5702, https://doi.org/10.1016/j.atmosenv.2004.04.024, 2004.

Burgos, M. A., Andrews, E., Titos, G., Alados-Arboledas, L., Baltensperger, U., Day, D., Jefferson, A., Kalivitis, N., Mihalopoulos, N., Sherman, J., Sun, J., Weingartner, E., and Zieger, P.: A global view on the effect of water uptake on aerosol particle light scattering, Sci. Data, 6, 157, https://doi.org/10.1038/s41597-019-0158-7, 2019a.

Burgos, M. A., Zieger, P., Andrews, E., Titos, G., Sherman, J., Jefferson, A., Mihalopoulos, N., Kouvarakis, G., Kalivitis, N., Sun, J., Alados-Arboledas, L., and Day, D.: Time series of aerosol light scattering coefficients and enhancement factors from tandem-humidified nephelometer at twenty-six stations between 1998 and 2017, ACTRiS Data Centre [data set], https://doi.org/10.21336/GEN.4, 2019b.

Cappa, C. D., Kolesar, K. R., Zhang, X., Atkinson, D. B., Pekour, M. S., Zaveri, R. A., Zelenyuk, A., and Zhang, Q.: Understanding the optical properties of ambient sub- and supermicron particulate matter: results from the CARES 2010 field study

in northern California, Atmos. Chem. Phys., 16, 6511–6535, https://doi.org/10.5194/acp-16-6511-2016, 2016.

Carslaw, K. S., Boucher, O., Spracklen, D. V., Mann, G. W., Rae, J. G. L., Woodward, S., and Kulmala, M.: A review of natural aerosol interactions and feedbacks within the Earth system, Atmos. Chem. Phys., 10, 1701–1737, https://doi.org/10.5194/acp-10-1701-2010, 2010.

Cazorla, A., Bahadur, R., Suski, K. J., Cahill, J. F., Chand, D., Schmid, B., Ramanathan, V., and Prather, K. A.: Relating aerosol absorption due to soot, organic carbon, and dust to emission sources determined from in-situ chemical measurements, Atmos. Chem. Phys., 13, 9337–9350, https://doi.org/10.5194/acp-13-9337-2013, 2013.

City of Arcata: Arcata General Plan, Environmental Quality and Management, Air Quality Element, Tech. rep., City of Arcata, https://www.cityofarcata.org/160/General-Plan (last access: 13 September 2022), 2008.

Collaud Coen, M., Weingartner, E., Nyeki, S., Cozic, J., Henning, S., Verheggen, B., Gehrig, R., and Baltensperger, U.: Long-term trend analysis of aerosol variables at the high-alpine site Jungfraujoch, J. Geophys. Res.-Atmos., 112, D13213, https://doi.org/10.1029/2006JD007995, 2007.

Collaud Coen, M., Andrews, E., Alastuey, A., Arsov, T. P., Backman, J., Brem, B. T., Bukowiecki, N., Couret, C., Eleftheriadis, K., Flentje, H., Fiebig, M., Gysel-Beer, M., Hand, J. L., Hoffer, A., Hooda, R., Hueglin, C., Joubert, W., Keywood, M., Kim, J. E., Kim, S.-W., Labuschagne, C., Lin, N.-H., Lin, Y., Lund Myhre, C., Luoma, K., Lyamani, H., Marinoni, A., Mayol-Bracero, O. L., Mihalopoulos, N., Pandolfi, M., Prats, N., Prenni, A. J., Putaud, J.-P., Ries, L., Reisen, F., Sellegri, K., Sharma, S., Sheridan, P., Sherman, J. P., Sun, J., Titos, G., Torres, E., Tuch, T., Weller, R., Wiedensohler, A., Zieger, P., and Laj, P.: Multidecadal trend analysis of in situ aerosol radiative properties around the world, Atmos. Chem. Phys., 20, 8867–8908, https://doi.org/10.5194/acp-20-8867-2020, 2020.

Crocker, I. and NOAA GML: Meteorology Data, [Trinidad Head, California, United States (THD), Meteorology], NOAA National Centers for Environmental Information (NCEI) [data set], https://gml.noaa.gov/aftp/data/meteorology/in-situ/thd/ (last access: 13 September 2022), 2017.

Delene, D. J. and Ogren, J. A.: Variability of Aerosol Optical Properties at Four North American Surface Monitoring Sites, J. Atmos. Sci., 59, 1135–1150, https://doi.org/10.1175/1520-0469(2002)059<1135:VOAOPA>2.0.CO;2, 2002.

Fitzgerald, J. W.: Marine aerosols: A review, Atmos. Environ. A Gen., 25, 533–545, https://doi.org/10.1016/0960-1686(91)90050-H, 1991.

Gao, S., Hegg, D. A., Hobbs, P. V., Kirchstetter, T. W., Magi, B. I., and Sadilek, M.: Water-soluble organic components in aerosols associated with savanna fires in southern Africa: Identification, evolution, and distribution, J. Geophys. Res.-Atmos., 108, 8491, https://doi.org/10.1029/2002JD002324, 2003.

Hallar, A. G., Petersen, R., Andrews, E., Michalsky, J., McCubbin, I. B., and Ogren, J. A.: Contributions of dust and biomass burning to aerosols at a Colorado mountain-top site, Atmos. Chem. Phys., 15, 13665–13679, https://doi.org/10.5194/acp-15-13665-2015, 2015.

Hodshire, A. L., Campuzano-Jost, P., Kodros, J. K., Croft, B., Nault, B. A., Schroder, J. C., Jimenez, J. L., and Pierce, J. R.: The potential role of methanesulfonic acid (MSA) in aerosol formation and growth and the associated radiative forcings, Atmos. Chem. Phys., 19, 3137–3160, https://doi.org/10.5194/acp-19-3137-2019, 2019.

IPCC: Climate Change 2013: The Physical Science Basis. Contribution of Working Group I to the Fifth Assessment Report of the Intergovernmental Panel on Climate Change, edited by: Stocker, T. F., Quin, D., Plattner, G. K., Tignor, M. M. B., Allen, S. K., Boschung, J., Nauels, A., Xia, Y., Bex, V., and Midgley, P. M., Cambridge University Press, Cambridge, United Kingdom and New York, NY, USA, https://doi.org/10.1017/CBO9781107415324, 2013.

Jaeglé, L., Quinn, P. K., Bates, T. S., Alexander, B., and Lin, J.-T.: Global distribution of sea salt aerosols: new constraints from in situ and remote sensing observations, Atmos. Chem. Phys., 11, 3137–3157, https://doi.org/10.5194/acp-11-3137-2011, 2011.

Jennings, S. G., Kleefeld, C., O'Dowd, C. D., Junker, C., Spain, T. G., O'Brien, P., Roddy, A. F., and O'Connor, T. C.: Mace Head Atmospheric Research Station – characterization of aerosol radiative parameters, Boreal Env. Res., 8, 303–314, 2003.

Katich, J. M., Samset, B. H., Bui, T. P., Dollner, M., Froyd, K. D., Campuzano-Jost, P., Nault, B. A., Schroder, J. C., Weinzierl, B., and Schwarz, J. P.: Strong Contrast in Remote Black Carbon Aerosol Loadings Between the Atlantic and Pacific Basins, J. Geophys. Res.-Atmos., 123, 13386–13395, https://doi.org/10.1029/2018JD029206, 2018.

Leaitch, W. R., Kodros, J. K., Willis, M. D., Hanna, S., Schulz, H., Andrews, E., Bozem, H., Burkart, J., Hoor, P., Kolonjari, F., Ogren, J. A., Sharma, S., Si, M., von Salzen, K., Bertram, A. K., Herber, A., Abbatt, J. P. D., and Pierce, J. R.: Vertical profiles of light absorption and scattering associated with black carbon particle fractions in the springtime Arctic above 79° N, Atmos. Chem. Phys., 20, 10545–10563, https://doi.org/10.5194/acp-20-10545-2020, 2020.

López, J. F., Cachorro, V. E., and de Frutos, A. M.: Analysis of aerosol scattering properties measured by a nephelometer at a coastal-rural site in the Atlantic southwest of the Iberian Peninsula, J. Atmos. Sol.-Terr. Phy., 132, 48–63, https://doi.org/10.1016/j.jastp.2015.06.011, 2015.

Maßling, A., Wiedensohler, A., Busch, B., Neusüß, C., Quinn, P., Bates, T., and Covert, D.: Hygroscopic properties of different aerosol types over the Atlantic and Indian Oceans, Atmos. Chem. Phys., 3, 1377–1397, https://doi.org/10.5194/acp-3-1377-2003, 2003.

Mayer, K. J., Wang, X., Santander, M. V., Mitts, B. A., Sauer, J. S., Sultana, C. M., Cappa, C. D., and Prather, K. A.: Secondary Marine Aerosol Plays a Dominant Role over Primary Sea Spray Aerosol in Cloud Formation, ACS Cent. Sci., 6, 2259–2266, https://doi.org/10.1021/acscentsci.0c00793, 2020.

Millet, D. B., Goldstein, A. H., Allan, J. D., Bates, T. S., Boudries, H., Bower, K. N., Coe, H., Ma, Y., McKay, M., Quinn, P. K., Sullivan, A., Weber, R. J., and Worsnop, D. R.: Volatile organic compound measurements at Trinidad Head, California, during ITCT 2K2: Analysis of sources, atmospheric composition, and aerosol residence times, J. Geophys. Res.-Atmos., 109, D23S16, https://doi.org/10.1029/2003JD004026, 2004.

Müller, T., Henzing, J. S., de Leeuw, G., Wiedensohler, A., Alastuey, A., Angelov, H., Bizjak, M., Collaud Coen, M., Engström, J. E., Gruening, C., Hillamo, R., Hoffer, A., Imre, K.,

Ivanow, P., Jennings, G., Sun, J. Y., Kalivitis, N., Karlsson, H., Komppula, M., Laj, P., Li, S.-M., Lunder, C., Marinoni, A., Martins dos Santos, S., Moerman, M., Nowak, A., Ogren, J. A., Petzold, A., Pichon, J. M., Rodriguez, S., Sharma, S., Sheridan, P. J., Teinilä, K., Tuch, T., Viana, M., Virkkula, A., Weingartner, E., Wilhelm, R., and Wang, Y. Q.: Characterization and intercomparison of aerosol absorption photometers: result of two intercomparison workshops, Atmos. Meas. Tech., 4, 245–268, https://doi.org/10.5194/amt-4-245-2011, 2011.

Murphy, D. M., Anderson, J. R., Quinn, P. K., McInnes, L. M., Brechtel, F. J., Kreidenweis, S. M., Middlebrook, A. M., Pósfai, M., Thomson, D. S., and Buseck, P. R.: Influence of sea-salt on aerosol radiative properties in the Southern Ocean marine boundary layer, Nature, 392, 62–65, https://doi.org/10.1038/32138, 1998.

Murphy, D. M., Capps, S. L., Daniel, J. S., Frost, G. J., and White, W. H.: Weekly patterns of aerosol in the United States, Atmos. Chem. Phys., 8, 2729–2739, https://doi.org/10.5194/acp-8-2729-2008, 2008.

Norris, G., Duvall, R., Brown, S., and Bai, S.: EPA Positive Matrix Factorization (PMF) 5.0 Fundamentals and User Guide, Tech. Rep. EPA/600/R-14/108; STI-910511-5594-UG, April, U.S. Environmental Protection Agency Office of Research and Development, Washington D.C., https://www.epa.gov/sites/default/files/2015-02/documents/pmf_5.0_user_guide.pdf (last access: 27 October 2022), 2014.

O'Dowd, C., Ceburnis, D., Ovadnevaite, J., Martucci, G., Bialek, J., Monahan, C., Berresheim, H., Vaishya, A., Grigas, T., Jennings, S. G., McVeigh, P., Varghese, S., Flanagan, R., Martin, D., Moran, E., Lambkin, K., Semmler, T., Perrino, C., and McGrath, R.: The Eyjafjallajökull ash plume – Part I: Physical, chemical and optical characteristics, Atmos. Environ., 48, 129–142, https://doi.org/10.1016/j.atmosenv.2011.07.004, 2012.

O'Dowd, C., Ceburnis, D., Ovadnevaite, J., Vaishya, A., Rinaldi, M., and Facchini, M. C.: Do anthropogenic, continental or coastal aerosol sources impact on a marine aerosol signature at Mace Head?, Atmos. Chem. Phys., 14, 10687–10704, https://doi.org/10.5194/acp-14-10687-2014, 2014.

O'Dowd, C. D. and de Leeuw, G.: Marine aerosol production: a review of the current knowledge, Philos. T. Roy. Soc. A, 365, 1753–1774, https://doi.org/10.1098/rsta.2007.2043, 2007.

Ogren, J. A.: Comment on "Calibration and Intercomparison of Filter-Based Measurements of Visible Light Absorption by Aerosols", Aerosol Sci. Tech., 44, 589–591, https://doi.org/10.1080/02786826.2010.482111, 2010.

Ogren, J. A., Wendell, J., Andrews, E., and Sheridan, P. J.: Continuous light absorption photometer for long-term studies, Atmos. Meas. Tech., 10, 4805–4818, https://doi.org/10.5194/amt-10-4805-2017, 2017.

Paatero, P.: Least squares formulation of robust non-negative factor analysis, Chemometr. Intell. Lab., 37, 23–35, https://doi.org/10.1016/S0169-7439(96)00044-5, 1997.

Paatero, P. and Tapper, U.: Analysis of different modes of factor analysis as least squares fit problems, Chemometr. Intell. Lab., 18, 183–194, https://doi.org/10.1016/0169-7439(93)80055-M, 1993.

Paatero, P. and Tapper, U.: Positive matrix factorization: A non-negative factor model with optimal utilization of er-

ror estimates of data values, Environmetrics, 5, 111–126, https://doi.org/10.1002/env.3170050203, 1994.

Paatero, P., Eberly, S., Brown, S. G., and Norris, G. A.: Methods for estimating uncertainty in factor analytic solutions, Atmos. Meas. Tech., 7, 781–797, https://doi.org/10.5194/amt-7-781-2014, 2014.

Parrish, D. D., Kondo, Y., Cooper, O. R., Brock, C. A., Jaffe, D. A., Trainer, M., Ogawa, T., Hübler, G., and Fehsenfeld, F. C.: Intercontinental Transport and Chemical Transformation 2002 (ITCT 2K2) and Pacific Exploration of Asian Continental Emission (PEACE) experiments: An overview of the 2002 winter and spring intensives, J. Geophys. Res.-Atmos., 109, D23S01, https://doi.org/10.1029/2004JD004980, 2004.

Quinn, P. K.: NOAA Regional Aerosol Sampling Stations, PMEL Atmospheric Chemistry Data Server [data set], https://saga.pmel.noaa.gov/data/ (last access: 13 September 2022), 2006.

Quinn, P. K., Bates, T. S., Miller, T. L., Coffman, D. J., Johnson, J. E., Harris, J. M., Ogren, J. A., Forbes, G., Anderson, T. L., Covert, D. S., and Rood, M. J.: Surface submicron aerosol chemical composition: What fraction is not sulfate?, J. Geophys. Res.-Atmos., 105, 6785–6805, https://doi.org/10.1029/1999JD901034, 2000.

Quinn, P. K., Miller, T. L., Bates, T. S., Ogren, J. A., Andrews, E., and Shaw, G. E.: A 3-year record of simultaneously measured aerosol chemical and optical properties at Barrow, Alaska, J. Geophys. Res.-Atmos., 107, AAC 8-1–AAC 8-15, https://doi.org/10.1029/2001JD001248, 2002.

Rinaldi, M., Decesari, S., Carbone, C., Finessi, E., Fuzzi, S., Ceburnis, D., O'Dowd, C. D., Sciare, J., Burrows, J. P., Vrekoussis, M., Ervens, B., Tsigaridis, K., and Facchini, M. C.: Evidence of a natural marine source of oxalic acid and a possible link to glyoxal, J. Geophys. Res.-Atmos., 116, D16204, https://doi.org/10.1029/2011JD015659, 2011.

Saarnio, K., Aurela, M., Timonen, H., Saarikoski, S., Teinilä, K., Mäkelä, T., Sofiev, M., Koskinen, J., Aalto, P. P., Kulmala, M., Kukkonen, J., and Hillamo, R.: Chemical composition of fine particles in fresh smoke plumes from boreal wild-land fires in Europe, Sci. Total Environ., 408, 2527–2542, https://doi.org/10.1016/j.scitotenv.2010.03.010, 2010.

Savoie, D. L. and Prospero, J. M.: Comparison of oceanic and continental sources of non-sea-salt sulphate over the Pacific Ocean, Nature, 339, 685–687, https://doi.org/10.1038/339685a0, 1989.

Schmeisser, L., Andrews, E., Ogren, J. A., Sheridan, P., Jefferson, A., Sharma, S., Kim, J. E., Sherman, J. P., Sorribas, M., Kalapov, I., Arsov, T., Angelov, C., Mayol-Bracero, O. L., Labuschagne, C., Kim, S.-W., Hoffer, A., Lin, N.-H., Chia, H.-P., Bergin, M., Sun, J., Liu, P., and Wu, H.: Classifying aerosol type using in situ surface spectral aerosol optical properties, Atmos. Chem. Phys., 17, 12097–12120, https://doi.org/10.5194/acp-17-12097-2017, 2017.

Schuster, G., Dubovik, O., and Holben, B.: Angstrom exponent and bimodal aerosol size distributions, J. Geophys. Res., 111, D07207, https://doi.org/10.1029/2005JD006328, 2006.

Sheridan, P., Andrews, E., Schmeisser, L., Vasel, B., and Ogren, J.: Aerosol Measurements at South Pole: Climatology and Impact of Local Contamination, Aerosol Air Qual. Res., 16, 855–872, https://doi.org/10.4209/aaqr.2015.05.0358, 2016.

Sheridan, P., Hageman, D., and NOAA GML: Earth System Research Laboratory Long-Term Surface Aerosol Measurements,

Version 1 [Trinidad Head, California, United States (THD), Aerosols], NOAA National Centers for Environmental Information (NCEI) [data set], https://doi.org/10.7289/V55T3HJF, 2017.

Sheridan, P. J., Delene, D. J., and Ogren, J. A.: Four years of continuous surface aerosol measurements from the Department of Energy's Atmospheric Radiation Measurement Program Southern Great Plains Cloud and Radiation Testbed site, J. Geophys. Res.-Atmos., 106, 20735–20747, https://doi.org/10.1029/2001JD000785, 2001.

Sherman, J. P., Sheridan, P. J., Ogren, J. A., Andrews, E., Hageman, D., Schmeisser, L., Jefferson, A., and Sharma, S.: A multi-year study of lower tropospheric aerosol variability and systematic relationships from four North American regions, Atmos. Chem. Phys., 15, 12487–12517, https://doi.org/10.5194/acp-15-12487-2015, 2015.

Sorribas, M., Ogren, J. A., Olmo, F. J., Quirantes, A., Fraile, R., Gil-Ojeda, M., and Alados-Arboledas, L.: Assessment of African desert dust episodes over the southwest Spain at sea level using in situ aerosol optical and microphysical properties, Tellus B, 67, 27482, https://doi.org/10.3402/tellusb.v67.27482, 2015.

Spracklen, D. V., Carslaw, K. S., Merikanto, J., Mann, G. W., Reddington, C. L., Pickering, S., Ogren, J. A., Andrews, E., Baltensperger, U., Weingartner, E., Boy, M., Kulmala, M., Laakso, L., Lihavainen, H., Kivekäs, N., Komppula, M., Mihalopoulos, N., Kouvarakis, G., Jennings, S. G., O'Dowd, C., Birmili, W., Wiedensohler, A., Weller, R., Gras, J., Laj, P., Sellegri, K., Bonn, B., Krejci, R., Laaksonen, A., Hamed, A., Minikin, A., Harrison, R. M., Talbot, R., and Sun, J.: Explaining global surface aerosol number concentrations in terms of primary emissions and particle formation, Atmos. Chem. Phys., 10, 4775–4793, https://doi.org/10.5194/acp-10-4775-2010, 2010.

Titos, G., Cazorla, A., Zieger, P., Andrews, E., Lyamani, H., Granados-Muñoz, M. J., Olmo, F. J., and Alados-Arboledas, L.: Effect of hygroscopic growth on the aerosol light-scattering coefficient: A review of measurements, techniques and error sources, Atmos. Environ., 141, 494–507, https://doi.org/10.1016/j.atmosenv.2016.07.021, 2016.

U.S. Geological Survey: The National Map – New data delivery homepage, advanced viewer, lidar visualization, USGS Numbered Series 2019-3032, U.S. Geological Survey, Reston, VA, https://doi.org/10.3133/fs20193032, 2019.

Vaishya, A., Jennings, S. G., and O'Dowd, C.: Seasonal Variation of the Aerosol Light Scattering Coefficient in Marine Air of the Northeast Atlantic, Adv. Meteorol., 2011, e170490, https://doi.org/10.1155/2011/170490, 2011.

Vaishya, A., Jennings, S. G., and O'Dowd, C.: Wind-driven influences on aerosol light scattering in northeast Atlantic air, Geophys. Res. Lett., 39, L05805, https://doi.org/10.1029/2011GL050556, 2012.

VanCuren, R. A., Cliff, S. S., Perry, K. D., and Jimenez-Cruz, M.: Asian continental aerosol persistence above the marine boundary layer over the eastern North Pacific: Continuous aerosol measurements from Intercontinental Transport and Chemical Transformation 2002 (ITCT 2K2), J. Geophys. Res.-Atmos., 110, D09S90, https://doi.org/10.1029/2004JD004973, 2005.

Virkkula, A., Teinilä, K., Hillamo, R., Kerminen, V.-M., Saarikoski, S., Aurela, M., Viidanoja, J., Paatero, J., Koponen, I. K., and Kulmala, M.: Chemical composition of boundary layer aerosol over the Atlantic Ocean and at an Antarctic site, Atmos. Chem. Phys., 6, 3407–3421, https://doi.org/10.5194/acp-6-3407-2006, 2006.

Vrekoussis, M., Liakakou, E., Koçak, M., Kubilay, N., Oikonomou, K., Sciare, J., and Mihalopoulos, N.: Seasonal variability of optical properties of aerosols in the Eastern Mediterranean, Atmos. Environ., 39, 7083–7094, https://doi.org/10.1016/j.atmosenv.2005.08.011, 2005.

Wang, J., Virkkula, A., Gao, Y., Lee, S., Shen, Y., Chi, X., Nie, W., Liu, Q., Xu, Z., Huang, X., Wang, T., Cui, L., and Ding, A.: Observations of aerosol optical properties at a coastal site in Hong Kong, South China, Atmos. Chem. Phys., 17, 2653–2671, https://doi.org/10.5194/acp-17-2653-2017, 2017.

Wang, R., Andrews, E., Balkanski, Y., Boucher, O., Myhre, G., Samset, B. H., Schulz, M., Schuster, G. L., Valari, M., and Tao, S.: Spatial Representativeness Error in the Ground-Level Observation Networks for Black Carbon Radiation Absorption, Geophys. Res. Lett., 45, 2106–2114, https://doi.org/10.1002/2017GL076817, 2018.

WMO/GAW: WMO/GAW Aerosol Measurement Procedures, Guidelines and Recommendations, 2nd edn., Report No. 227, World Meteorological Organization, Geneva, Switzerland, ISBN 978-92-63-11177-7, 2016.

Wood, R., Wyant, M., Bretherton, C. S., Rémillard, J., Kollias, P., Fletcher, J., Stemmler, J., de Szoeke, S., Yuter, S., Miller, M., Mechem, D., Tselioudis, G., Chiu, J. C., Mann, J. A. L., O'Connor, E. J., Hogan, R. J., Dong, X., Miller, M., Ghate, V., Jefferson, A., Min, Q., Minnis, P., Palikonda, R., Albrecht, B., Luke, E., Hannay, C., and Lin, Y.: Clouds, aerosols, and precipitation in the marine boundry layer: An ARM Mobile Facility Deployment, B. Am. Meteorol. Soc., 96, 419–440, https://doi.org/10.1175/BAMS-D-13-00180.1, 2015.

Yoon, Y. J., Ceburnis, D., Cavalli, F., Jourdan, O., Putaud, J. P., Facchini, M. C., Decesari, S., Fuzzi, S., Sellegri, K., Jennings, S. G., and O'Dowd, C. D.: Seasonal characteristics of the physicochemical properties of North Atlantic marine atmospheric aerosols, J. Geophys. Res.-Atmos., 112, D04206, https://doi.org/10.1029/2005JD007044, 2007.

Zhou, S., Collier, S., Jaffe, D. A., Briggs, N. L., Hee, J., Sedlacek III, A. J., Kleinman, L., Onasch, T. B., and Zhang, Q.: Regional influence of wildfires on aerosol chemistry in the western US and insights into atmospheric aging of biomass burning organic aerosol, Atmos. Chem. Phys., 17, 2477–2493, https://doi.org/10.5194/acp-17-2477-2017, 2017.

Zieger, P., Fierz-Schmidhauser, R., Gysel, M., Ström, J., Henne, S., Yttri, K. E., Baltensperger, U., and Weingartner, E.: Effects of relative humidity on aerosol light scattering in the Arctic, Atmos. Chem. Phys., 10, 3875–3890, https://doi.org/10.5194/acp-10-3875-2010, 2010.

Zieger, P., Fierz-Schmidhauser, R., Poulain, L., Müller, T., Birmili, W., Spindler, G., Wiedensohler, A., Baltensperger, U., and Weingartner, E.: Influence of water uptake on the aerosol particle light scattering coefficients of the Central European aerosol, Tellus B, 66, 22716, https://doi.org/10.3402/tellusb.v66.22716, 2014.